

# Current Overview of Statistical Fiber Bundles Model and Its Application to Physics-based Reliability Analysis of Thin-film Dielectrics

James U. Gleaton<sup>1</sup>, David Han<sup>2</sup>, James D. Lynch<sup>3</sup>,  
 Hon Keung Tony Ng<sup>4</sup> and Fabrizio Ruggeri<sup>5</sup>

<sup>1</sup>*James U. Gleaton is Professor Emeritus, Department of Mathematics and Statistics, University of North Florida, Jacksonville, Florida, U.S.A. e-mail: jug\_head@earthlink.net.*

<sup>2</sup>*David Han is Associate Professor, Department of Management Science and Statistics, University of Texas at San Antonio, San Antonio, Texas, U.S.A. e-mail: David.Han@utsa.edu.*

<sup>3</sup>*James D. Lynch is Distinguished Professor Emeritus, Department of Statistics, University of South Carolina, Columbia, South Carolina, U.S.A. e-mail: lynch@stat.sc.edu.*

<sup>4</sup>*Hon Keung Tony Ng is Professor, Department of Statistical Science, Southern Methodist University, Dallas, Texas, U.S.A. e-mail: ngh@mail.smu.edu.*

<sup>5</sup>*Fabrizio Ruggeri is Research Director, CNR IMATI, Milano, Italy. e-mail: fabrizio@mi.imati.cnr.it.*

**Abstract:** In this paper, we present a critical overview of statistical fiber bundles models. We discuss relevant aspects, like assumptions and consequences stemming from models in the literature and propose new ones. This is accomplished by concentrating on both the physical and statistical aspects of a specific load-sharing example, the breakdown (BD) for circuits of capacitors and related dielectrics. For series and parallel/series circuits (series/parallel reliability systems) of ordinary capacitors, the load-sharing rules are derived from the electrical laws. This with the BD formalism is then used to obtain the BD distribution of the circuit. The BD distribution and Gibbs measure are given for a series circuit and the size effects are illustrated for simulations of series and parallel/series circuits. This is related to the finite weakest link adjustments for the BD distribution that arise in large series/parallel reliability load-sharing systems, such as dielectric BD, from their extreme value approximations.

An elementary but in-depth discussion of the physical aspects of  $\text{SiO}_2$  and  $\text{HfO}_2$  dielectrics and cell models is given. This is used to study a load-sharing cell model for the BD of  $\text{HfO}_2$  dielectrics and the BD formalism. The latter study is based on an analysis of Kim and Lee (2004)'s data for such dielectrics. Here, several BD distributions are compared in the analysis and proportional hazard regression models are used to study the BD formalism. In addition, some areas of open research are discussed.

**Keywords and phrases:** Electric circuits, hard breakdown, load-sharing system, proportional hazards model, soft breakdown.

## 0. Overall Introduction

Over the last sixty years, fiber bundle models (FBM) have played an indispensable role in “Modelling Critical and Catastrophic Phenomena.” The phrase in quotes is part of the title of a book on FBM ([Bhattacharyya and Chakrabarti, 2006](#)). This book consists of several tutorial introductory chapters, one of which is by [Kun et al. \(2006\)](#) entitled “Extensions of fiber bundle models,” where they state that “The fiber bundle model is one of the most important theoretical approaches to investigate the fracture and breakdown (BD) of disordered media extensively used both by the engineering and physics community.” The chapters after the introductory chapters are specialized applications of the FBM in the geosciences.

A related reference that is an excellent introduction to FBM and accessible to non-physicists is [Hansen, Hemmer and Pradhan \(2015\)](#)’s book entitled “The Fiber Bundle Model: Modeling Failure in Materials.” Another is [Bažant and Le \(2017\)](#)’s book entitled “Probabilistic Mechanics of Quasibrittle Structures – Strength, Lifetime, and Size Effect.”

The point of the current overview paper is to present a friendly introduction of this important topic to those statisticians that are not familiar with it. This is accomplished by concentrating on both the physical and statistical aspects of a specific load-sharing example, the BD for circuits of capacitors and related dielectrics. By concentrating on this specific situation, the presentation can be done in an axiomatic framework that is more comfortable to statisticians and probabilists; e.g., the load-sharing rule can be derived from first principles and the physical aspects of dielectric breakdown are discussed at an elementary level. On the other hand, material scientists also might find the overview enlightening; the statistical aspects presentation is self-contained.

The starting point of FBM originated with [Daniels \(1945\)](#) seminal work on the distribution of breaking strength of a bundle of threads. Here, in equilibrium, Hooke’s law is  $\sigma = Y\varepsilon$ , where  $\sigma, \varepsilon$  and  $Y$  are, respectively, *stress*, *strain* and *Young’s modulus*. For homogeneous bundles, where all the threads have the same Young’s modulus, Hooke’s law leads to the equal load-sharing rule when all the threads have the same cross-sectional area and proportional load-sharing if they have different areas where the proportions depend on the cross-sectional areas.

These are equilibrium rules that are abruptly violated when a thread fails under increasing load. A thread breakage initiates a violent process, not easy to model, that can cause a cascade of thread failures. After this cascade, once the bundle is again in equilibrium, the surviving threads share the load equally or proportionally for a homogeneous bundle.

In Part I, we consider series circuits of capacitors to illustrate FBM. Much like stressed threads that store potential energy, capacitors are electrical devices that store electrical energy and series circuits of capacitors behave like bundles of threads. In addition, the capacitor law for a given capacitor,  $V = C^{-1}Q$ , where  $V$ ,  $C$  and  $Q$  are, respectively, the voltage, capacitance and charge for that capacitor is analogous to Hooke’s law and leads to the equal load-sharing

rule if all the capacitances are the same in the circuit. Besides series circuits of ordinary capacitors, we also discuss the electrical breakdown of thin dielectrics and cell models that have been used to model them. In particular, we discuss the load-sharing cell model where the thin dielectric is modeled as a parallel circuit of cells and where the cell consists of a series circuit of nano-capacitors subject to the electrical laws for ordinary capacitors. This conceptualism leads to a weakest-link chain-of bundles/cell model where, for an infinite chain, extreme value asymptotics leads to a Weibull distribution for the BD distribution for the dielectric. Lack of fit for the Weibull is considered a size effect and leads to consideration of the finite-weakest-link model to account for this.

In Part II, we consider the statistical aspects of circuits of ordinary capacitors and thin dielectrics. Statistical analyses of such circuits and dielectrics are given and related size effects are illustrated and discussed. We give a critical overview of the model assumptions and propose modifications.

We close the Overall Introduction with a discussion of further background and other applications of FBM. In addition to the physics-based reliability analysis of semiconductor dielectrics, there exist limitless applications of the fiber bundle models, many found in the fields of material science, mechanical and structural engineering, and nanotechnology. Its application to understand and explain the physical failure process has a long and rich history. During World War II, it was used to analyze the sudden and unexpected failure of the American Liberty cargo ships. They were the first ships built with hulls that were welded rather than riveted, and some of them broke in half without warning. Another catastrophic example is the hull failure of a Boeing 737 airplane during flight in April 1988 in Hawaii. An explosive decompression occurred and the airplane fuselage was ripped away mid-air. After the investigation based on the fiber bundle models, it was realized that the failure process had started long before as a small crack near a rivet due to metal fatigue initiated by crevice corrosion. The crack grew due to the cyclic pressure loading from flying and being on the ground.

Recently, [Mishnaevsky \(2013\)](#) used FBM for the micromechanics of wind turbine blade composites. The strength, stiffness and fatigue life of composite materials were predicted, and the microstructural effects and suitability of different groups of materials were analyzed for applications in wind turbine blades. [Pugno \(2014\)](#) reviewed the mechanics of nanotubes, graphene and related fibers. For designing super-strong carbon nanotube, graphene fibers and composites, FBM were applied to quantify the effect of thermodynamically unavoidable atomistic defects on the fracture strength. Using FBM, [Orgéas, Dumont and Corre \(2015\)](#) discussed the rheology of highly concentrated fiber suspensions. Polymer composites reinforced with fibers or fiber bundles are suitable for many aeronautic, automotive, shipbuilding, electrical, electronic, health and sports applications. Among these materials, sheet molding compounds, bulk molding compounds, glass mat thermoplastics and carbon mat thermoplastics are the subject of several ongoing research, and their structural properties with respect to the material reliability are understood using the fiber bundle models. More recently, [Boufass et al. \(2020\)](#) studied the composite material energy for the FBM when the fibers in the composite are randomly oriented. Also, [Leckey et al. \(2020\)](#) de-

scribed the construction of prediction intervals for the time that a given number of components fail in a load-sharing system. Their interest was in the successive failure of tension wires (the components) in prestressed concrete beams.

Although unconventional, FBM could also be applied to understand natural phenomena in which rapid mass movements are triggered. [Reiweger et al. \(2009\)](#) used a FBM to describe a slab snow avalanche, the most dangerous snow avalanches, accounting for 99% of fatal avalanches in Canada during the period 1972–1991. The slab snow avalanche presupposes the existence of a weak layer below the surface, which triggers a complete sheet of snow to slide. Further down the slope, the slab may break up into smaller pieces.

Among different types and causes of landslides, some landslide models involve fiber bundles. Like the slab snow avalanches, a buried weak layer may cause a shallow landslide to occur. The weak layer is usually caused by infiltration of water, by rapid snow melting, or by heavy rainfall. This results in reduction of the soil strength. The water-induced weakening is modeled by making the strength distribution of the fibers in the fiber bundle depend on the water content. To estimate the time to failure, [Lehmann and Or \(2012\)](#) modelled the time-dependent water infiltration for a given rainfall. As roots have a stabilizing effect in soil and may inhibit landslides, [Cohen, Schwarz and Or \(2011\)](#) developed FBM for shallow landslides by treating roots as fibers.

Finally, a Markov chain random walk on a graph is basic to well-defining local-load sharing rules since these rules do not fully describe the load-sharing over all possible configurations of component failures. In addition, it also gives a way to obtain the “equilibrium” joint distribution of the states of the components of the related FBM. To do this, let the nodes in the Markov chain graph correspond to the components in the FBM where the edges indicate how the load is transferred locally. The local-load sharing rules define the one-step transition probabilities of the chain. Consider a set of surviving components in the FBM and their corresponding nodes which are now considered as absorbing states of the chain. The absorption probabilities are used to extend the local load-sharing rule to this set of components.

The above is a generic model for the failure of a FBM network based on the Markov chain graph. As the load increases components/nodes fail, one considers the BD of the network. This with the components/nodes’ BD distributions can be used to construct the Gibbs measure for the state of the network (Section 7.3). The Gibbs measure indicates what routes are available, if any, between two components.

This approach was used to determine the shape of a bundle in [Li, Gleaton and Lynch \(2019\)](#) where  $P$  bundle failed when there was a route/crack across bundle. This network model may also have implications for the reliability of certain types of nanosensors. [Ebrahimi, McCullough and Xiao \(2013a,b\)](#) used a lattice structure for the nanosensor where the sensor fails when there is no conductive route across the lattice but they use a percolation model to produce a conductive route. We do not elaborate on this abstraction in the sequel.

## 1. Part I Introduction: Physical Aspects

In the next section, we discuss plate capacitors (devices used to store an electric charge) and the electrical laws for series, parallel and parallel/series circuits of ordinary capacitors and the dynamic behavior of the charge and voltage distribution in a series circuit. In Sections 3 and 4, the physical aspects of the BD of thin-film dielectrics and cell models for this are presented and the size effects for the load-sharing cell models are discussed.

## 2. Electrical Circuits of Ordinary Capacitors

Here, we give a brief review regarding traditional circuits of ordinary capacitors where current is described as a flow in the classical theory of circuits. We distinguish this from later sections regarding thin dielectrics that are solid-state electronic devices. For such devices, the flow analogy is only approximate because, at the nanoscale, quantum effects have to be taken into consideration. This is discussed in Section 3. The discussion of capacitors, resistors, and classic electric circuits that follows is based on [Jones \(1971\)](#).

Plate type capacitors are discussed in Section 2.1 while, in Section 2.2, the electrical laws for parallel and series circuits of ordinary capacitors and the behavior of the charge distribution on a series circuit are given.

### 2.1. Electrical Laws For Circuits Of Capacitors

The capacitance of a plate type capacitor, with plate area  $A$ , separation  $d$  between the plates and filled with a vacuum (or air, approximately), is a structural constant of the device given by

$$C = \frac{\varepsilon_0 A}{d}. \quad (2.1)$$

Here,  $\varepsilon_0$  is the electric permittivity of free space,  $8.85418 \times 10^{-12} \frac{\text{coul}^2}{\text{nt}\cdot\text{m}^2}$ . If we replace the vacuum (air) between the plates by a dielectric material with permittivity  $\varepsilon = \kappa\varepsilon_0$ , the capacitance will be larger by a factor  $\kappa (> 1)$ , the *relative permittivity (dielectric constant)* of the dielectric material. Thus,

$$C = \frac{\kappa\varepsilon_0 A}{d}. \quad (2.2)$$

For silicon dioxide ( $\text{SiO}_2$ ), the dielectric constant is approximately 3.9. For silicon (Si), the dielectric constant is approximately 11.0 to 12.0 and that of hafnium dioxide ( $\text{HfO}_2$ ), a *high- $\kappa$  dielectric*, is 25. Notice that, from Eqs. (2.1) and (2.2), part of the variation of the capacitance,  $C$ , is captured in the manufacturing variation of  $A$  and  $d$  of the capacitor.

It is instructive to let  $A = A_n = nA_0$  and  $d = d_m = md_0$  in Eqs. (2.1) and (2.2), where  $n$  and  $m$  are positive integers and  $A_0$  and  $d_0$  are positive constants.

Then, Eqs. (2.1) and (2.2) become

$$C_{n,m} \propto \frac{A_n}{d_m} = \frac{nA_0}{md_0}. \quad (2.3)$$

This indicates that the capacitance increases in cross-sectional area  $nA_0$  and decreasing in thickness  $md_0$ . These relationships are analogues of the electrical circuit laws for capacitors where the capacitance of a parallel systems of capacitors is the sum of the individual components capacitance and for series systems it is the harmonic sum. These circuit laws are discussed in the next section.

## 2.2. Conservation Laws for Series and Parallel Circuits

Below we state the capacitor laws for series and parallel circuits. The results are based on the *capacitance law* of the *capacitance*,  $C$ , of a capacitor in terms of *voltage*,  $V$ , and *charge*,  $Q$ , across it and the conservation laws of energy/voltage and of charge/current.

### The Capacitance Law

$$C = Q/V. \quad (2.4)$$

**Remark:** The equivalent form of the law

$$V = C^{-1}Q, \quad (2.5)$$

is analogous to Hooke's Law where  $C^{-1}$  is Young's modulus, the voltage is the force/stress and the charge is the extension/strain.

### 2.2.1. Conservation Laws for Series and Parallel Circuits

In this and the next subsection, we just highlight the conservation laws relevant to capacitor circuits and the consequences. For this,  $C_i$ ,  $Q_i$  and  $V_i$  are, respectively, the capacitance of capacitor  $i$ , the charge at it and the voltage across it for  $i = 1, 2, \dots, m$  where  $C_i = Q_i/V_i$ . We use  $V_{\Pi}$ ,  $V_{\Pi}$ ,  $Q_{\Pi}$ , and  $Q_{\Pi}$  to denote the respective voltages and charges of series circuits ( $\Pi$ ) and parallel circuits ( $\Pi$ ).

In a series circuit, its voltage is the sum of the voltages across all the capacitors, whereas its charge equals the ones in each capacitor.

### Series Circuit Laws

$$\text{Series Voltage Law} \quad V_{\Pi} = \sum_{i=1}^m V_i. \quad (2.6)$$

$$\text{Series Charge Law} \quad Q_{\Pi} = Q_i \text{ for } i = 1, 2, \dots, m. \quad (2.7)$$

In a parallel circuit, its charge is the sum of the charges across all the capacitors, whereas its voltage equals the ones in each capacitor.

### Parallel Circuit Laws

$$\text{Parallel Charge Law} \quad Q_{\Pi} = \sum_{i=1}^m Q_i. \quad (2.8)$$

$$\text{Parallel Voltage Law} \quad V_{\Pi} = V_i \text{ for } i = 1, 2, \dots, m. \quad (2.9)$$

### 2.2.2. Consequences of the Conservation Laws: The Capacitor Laws

#### Series Capacitor Law

$$\sum_{i=1}^m \frac{1}{C_i} = \sum_{i=1}^m \frac{V_i}{Q_{\Pi}} = \frac{V_{\Pi}}{Q_{\Pi}} \equiv \frac{1}{C_{\Pi}}, \text{ i.e., } C_{\Pi} = 1 \left/ \sum_{i=1}^m \frac{1}{C_i} \right. . \quad (2.10)$$

Justification Identity (2.10) follows from (2.6) and (2.7) since  $C_i = Q_i/V_i = Q_{\Pi}/V_i$ , and so,

$$\frac{1}{C_i} = \frac{V_i}{Q_{\Pi}}. \quad \square$$

#### Parallel Capacitor Law

$$\sum_{i=1}^m C_i = \sum_{i=1}^m \frac{Q_i}{V_{\Pi}} = \frac{Q_{\Pi}}{V_{\Pi}} = C_{\Pi}. \quad (2.11)$$

Justification Identity (2.11) follows from (2.8) and (2.9) since  $C_i = Q_i/V_i = Q_{\Pi}/V_{\Pi}$ .  $\square$

**Comments:** Consider a plate capacitor whose capacitance  $C_{1,1}$  is given by (2.3) with  $m = 1 = n$ . If we increase the thickness of the capacitor by a factor  $m$ , the capacitance is  $C_{1,m}$  and this stacking of plate capacitors is equivalent to a series circuit of capacitors with capacitance  $C_{1,1}$  by the series capacitor law (2.10). Similarly, by increasing the plate area by a factor  $n$ , the capacitance is  $C_{n,1}$  and this increase in plate area is equivalent to a parallel circuit of capacitors with capacitance  $C_{1,1}$  by the parallel capacitor law (2.11).

### 2.2.3. Parallel and Series Circuits of Capacitors with the Same Capacitance

In this subsection, we consider series and parallel circuits of  $m$  capacitors with the same capacitance,  $C$ . In Facts A and B below, we see that the load-sharing on each capacitor in the circuit is the same (the so-called equal load-sharing rule) in terms of the voltage and charge, respectively, for series and parallel circuits.

**Fact A.** Consider a series circuit of  $m$  capacitors each having the same capacitance,  $C$ , where the voltage across the circuit is  $V_{\Pi}$ . Then, the voltage across the  $i$ th capacitor is  $V_i = V_{\Pi}/m$ .

Justification From (2.7),  $C = C_i = \frac{Q_i}{V_i} = \frac{Q_{\Pi}}{V_i}$ . Thus,  $V_i = Q_{\Pi}C \equiv V$  and, from (2.6),  $V_{\Pi} = \sum_{i=1}^m V_i = mV$ . So,  $V_i = V = \frac{V_{\Pi}}{m}$ .  $\square$

Remark 2.2.3: (i) Note that as capacitors fail, the circuit is still a series one but the failed capacitors become now conductors. It follows that the voltage across each of the working capacitors is  $\frac{V_{\Pi}}{M}$ , where  $M$  is the number of working capacitors. This is the *equal load-sharing rule* and the series circuit is a *load-sharing system* in terms of the voltage. (ii) If one has capacitors of  $k < m$

different capacitances, the above argument can be modified to show how the voltage/load is distributed proportionally among the different types.  $\square$

**Fact B.** Consider a parallel circuit of capacitors each having the same capacitance,  $C$ , where the charge across the circuit is  $V_{II}$ . Then, the charge across the  $i$ th capacitor is  $Q_i = Q_{II}/m$ .

Justification From (2.9),  $C = C_i = \frac{Q_i}{V_i} = \frac{Q_i}{V_{II}}$ . Thus,  $Q_i = CV_{II} \equiv Q$  and, from (2.8),  $Q_{II} = \sum_{i=1}^m Q_i = mQ$ . So,  $Q_i = Q = \frac{Q_{II}}{m}$ .  $\square$

#### 2.2.4. Behavior of the Charge and Voltage Load Distributions for Series Circuits of Capacitors

The previous electrical laws were valid for the equilibrium case. Here, we study the dynamic behavior of the charge and voltage load distributions for a series circuit of capacitors and how they converge to equilibrium, based on Kirchoff's circuit laws (Jones, 1971).

First, consider a series circuit loop in which there are two capacitors with equal capacitance  $C$ , a battery with electromotive force  $V$ , and a switch. Let  $r$  denote the (nearly negligible) resistance of the circuit wires. If the resistance of the circuit wires were 0, then the approach to equilibrium would be instantaneous. Also, when the breakdown of a capacitor happens, the capacitor ceases to be a capacitor and becomes a resistor. An ohmic (linear) resistor is a passive circuit component that limits the flow of electric current and dissipates electromagnetic energy as heat. The relationship between the applied voltage (electromotive force),  $V$ , and the current,  $I$ , flowing through the circuit is called Ohm's Law,  $V = IR$ , where  $R$  is a characteristic, called resistance, of the resistor – the greater the value of  $R$ , the lower the current for a given voltage. The energy dissipation equation for the resistor is  $P = I^2R$ , where  $P$  is the power or energy dissipated per unit time.

When the circuit is closed, the equation governing the charge distribution's,  $q(t)$ , approach to equilibrium is:

$$V = r \frac{dq}{dt} + \frac{2}{C}q.$$

The solution to this equation is

$$q(t) = \frac{CV}{2} \left( 1 - e^{-\frac{2t}{rC}} \right) \equiv CV(t),$$

for  $t \geq 0$  where  $V(t)$  is the voltage load at a capacitor. Then, the current is

$$\dot{q}(t) = \frac{V}{r} e^{-\frac{2t}{rC}}.$$

If one of the capacitors fails, becoming a resistor with resistance  $R_1$ , the differential equation governing the return to equilibrium is:

$$V = (r + R_1) \frac{dq}{dt} + \frac{1}{C}q.$$

The solution to this equation is

$$q(t) = CV \left( 1 - e^{-\frac{t}{(r+R_1)C}} \right),$$

and the current in the circuit as the system approaches equilibrium is

$$\dot{q}(t) = \frac{V}{r+R_1} e^{-\frac{t}{(r+R_1)C}}.$$

If the second capacitor fails, it becomes a resistor with resistance  $R_2$ . The current in the circuit is then constant:

$$\dot{q}(t) = \frac{V}{r+R_1+R_2}.$$

Note that we cannot assume that the two new resistors have equal resistances. The capacitors may have had equal capacitances, but when they fail, they do not necessarily fail in the exact same way. The resistance depends on the breakdown path(s) through the dielectric insulating material that causes capacitor failure. Further discussion of this is in Section 3.

For a series circuit with  $k (\geq 2)$  capacitors, each with capacitance  $C$ , the equation governing the approach to equilibrium, after  $j < k$  capacitors fail, is

$$V = (r + R_T) \frac{dq}{dt} + \frac{k-j}{C} q,$$

where  $R_T = \sum_{i=1}^j R_i$ . The solution is

$$q(t) = \frac{CV}{k} \left( 1 - e^{-\frac{(k-j)t}{(r+R_T)C}} \right) \equiv CV(t),$$

with current

$$\dot{q}(t) = \frac{V}{r+R_T} e^{-\frac{(k-j)t}{(r+R_T)C}}.$$

In general, if  $k$  is the number of working capacitors, the equilibrium charges and voltage loads at the working capacitors are

$$q(t) \rightarrow \frac{CV}{k} \equiv Q \text{ and } V(t) \rightarrow \frac{V}{k},$$

where  $V/k$  is the equal load-sharing rule.

### 3. BD of Thin-Film Dielectrics

We are considering the breakdown mechanisms of a thin film dielectric. The earlier type of dielectric used in electronic circuits, silicon dioxide, is generated on a metal substrate by a chemical vapor deposition process (Chu, 2014). The deposition process is usually performed at relatively low temperatures to avoid defect formation, diffusion, and degradation of the metal layers.

However, at lower temperatures, more impurities are generated in the silicon dioxide. The vapor involved in the deposition process is a mixture of silane ( $\text{SiH}_4$ ) and nitrous oxide ( $\text{N}_2\text{O}$ ) in nitrogen. The result is that there is a relatively small number of silanol ( $\text{SiOH}$ ) and water sites in the silicon dioxide thin film.

Due to the effects of these impurities on the reliability of the dielectric and the need for thinner dielectric films in newer electronic devices, materials other than silicon dioxide have been evaluated in recent years. One promising material that appears to outperform others (Bersuker et al., 2007; Iglesias et al., 2011; McKenna and Shluger, 2011; Pirrotta et al., 2013) is hafnium oxide (hafnia).

The following brief discussion of some concepts from solid-state physics follows Jones (1971). We begin with a discussion of the quantum band structure of crystalline solids. In the next subsection, there is a basic discussion of the quantum band structure of crystalline solids. Subsequent subsections include a discussion of the electronic structure of a thin-film silicon dioxide dielectric layer, followed by a discussion of the structure of a thin-film hafnium oxide layer, on a silicon substrate. Afterward, the conduction mechanisms through such dielectrics are discussed. Finally, there is a discussion of the occurrence of soft- and hard-breakdowns of dielectrics.

### 3.1. *Quantum Theory of Electron States in Solids*

For an isolated atom, atomic energy levels are degenerate (Jones, 1971), i.e., there may be several electrons with the same energy but different values of the other quantum numbers. A level may be of degeneracy 2, 8, 18, 32, etc. When the atom is embedded in a crystal of the same element, with perhaps  $10^{19}$  atoms, interactions among the atoms removes the degeneracy, spreading out the states. For an energy level of degeneracy  $m$  in a crystal of  $N$  atoms, the level is spread into  $Nm$  states which are close to each other in energy, so that the level may be approximated by a continuous band.

In an insulating material, there is a full band (all states are occupied), called the valence band, separated by a (relatively large) energy gap from the higher and empty conducting band. An electron in the valence band would need to absorb an amount of energy at least as large as the band gap to jump to a state in the conduction band. In a semiconducting material, there is a smaller band gap, so that those thermal excitations may be sufficient to cause electrons to jump into the conduction band and be able to conduct current. In a metal, the valence band is full, and the conduction band is partially full so that electrons in that band are able to conduct current when an electric field is applied across the metal crystal.

### 3.2. *The Two Dielectric Materials Being Examined*

#### 3.2.1. *Structure of Silicon Dioxide Thin Films*

The electronic band structure of solids also applies to molecular solids, as well as to atomic solids, and to amorphous solids, as well as crystalline solids. Silicon

dioxide, in the amorphous form used in electronic devices, also has a band structure (Nekrashevish and Gritsenko, 2014).

A thin film of silicon dioxide is dielectric (insulating). With no applied electric field across the dielectric, the valence band in the thin film is fully occupied, while the conduction band is empty. The applied field would need to be relatively strong to give enough energy to a valence band electron to enable it to jump to a state in the conduction band.

In a  $\text{SiO}_2$  thin film with impurities, however, there may be additional states, called trapping states (Alam et al., 1999; Alam, Weir and Silverman, 2002; Houssa et al., 2000) located in the band gap between the valence band and the conduction band. An electron in the valence band may gain enough energy, perhaps from the applied electric field, to jump to one of these intermediate states, even if it does not gain enough energy to jump to a state in the conduction band. An electron in the conduction band could lose energy, perhaps to thermal excitation of the dielectric, and fall into one of the trapping states.

With silanol impurities in the dielectric, there will be mobile protons (Houssa et al., 2000), which can jump from a silanol site in the film to a neighboring  $\text{SiO}_2$  site as the energy input from the applied electric field leads to disruption and re-establishment of atomic bonds. Thus, trapping sites in the dielectric are not fixed, but can rearrange themselves under the influence of an applied electric field. The mobility of these protons can then generate percolation paths across the dielectric. A percolation path is a sequence of traps spanning the distance from the cathode to the anode. The number of traps in a percolation path can vary, depending on the thickness of the dielectric, the density of trapping sites in the dielectric, and the applied electric field, which, as stated above, can cause traps to shift from one site to another.

### 3.2.2. Structure of Hafnium Oxide Thin Films

Recent developments in electronic technology have motivated a search for more efficient dielectric materials than silicon dioxide, in order to allow for smaller, more efficient electronic components. In this context, more efficient means three things: a) the dielectric material needs to have a higher relative permittivity, leading to the same performance (capacitance, e.g.) with a thinner layer of material, b) a relatively large band gap between the valence band and the conduction band, and c) higher reliability – a longer time to breakdown and a higher breakdown voltage.

One promising candidate for such a material is hafnium oxide ( $\text{HfO}_2$ ), or hafnia (Lee, Jeon and Kwong, 2002; Smirnova et al., 2008; Zhang et al., 2019). This material has a much higher relative permittivity than silicon dioxide ( $\kappa \cong 25$  for  $\text{HfO}_2$ , as opposed to  $\kappa \cong 3.8$  for  $\text{SiO}_2$ ). The band gap for  $\text{HfO}_2$  is approximately 5.68 eV, which, though smaller than the band gap for  $\text{SiO}_2$  (8.9 eV) is large enough for use in similar electronic applications. Also, as discussed below, the characteristics of trapping sites and the relative strengths of the charge transport mechanisms differ from those of  $\text{SiO}_2$  in favorable ways.

There are different mechanisms used for creating a hafnia layer on a silicon substrate. One method involves vapor deposition using various organometallic compounds as precursors (Smirnova et al., 2008). These vapors were transported to the substrate by argon (inert) carrier stream at a flow rate of 50–200 cm<sup>3</sup>/min. The films were found, using infrared examination and energy-dispersive X-ray spectroscopy, to contain residual organics. The organics were removed by annealing the hafnia at 1070°K. It was then found that the films grown from hafnium dipivaloylmethanate were free of organics to the limit of the IR spectroscopy. The resulting films were then examined using infrared radiation, X-ray photoelectron detection, energy-dispersive X-ray spectroscopy, X-ray diffraction, ellipsometry, and electrophysical methods. It was found that the films also contained HfSi and HfSiO<sub>4</sub> due to chemical reactions at the interface with the silicon substrate. This interface layer would affect the current conduction mechanisms of the hafnia.

Annealing the hafnia removes some of the impurities but also changes its structure. It produces a dielectric layer with a mixture of amorphous and polycrystalline forms (Zhang et al., 2019). Within the microcrystals (or grains), the hafnia has a regular cubic lattice structure, with few or no defects or deformities. Within the amorphous phase, there are randomly scattered irregularities, in the form of elongated hafnium-oxygen bonds. These elongated bonds are also more concentrated in the grain boundaries (Bersuker et al., 2007; Iglesias et al., 2011; Pirrotta et al., 2013), between adjacent grains and between grains and the amorphous part of the dielectric.

Bersuker et al. (2007) examined electron trapping under constant voltage stress. They found evidence of two types of trapping:

- a) Fast trapping occurs when electrons tunnel from the cathode to pre-existing (as grown) defects; these defects occur primarily at grain boundaries, and consist of elongated hafnium-oxygen bonds, due to distortion/dislocation of the crystalline structure at the boundaries. These dislocations contain under-coordinated oxygen ions (an ion's coordination number is the number of adjacent oppositely-charged ions in the regular crystal lattice), resulting in electron traps with energy levels within the band gap. These location sites are also locally positively charged, acting to attract electrons.
- b) Slow trapping occurs when thermally activated trapped electrons migrate to unoccupied traps.

Iglesias et al. (2011) used conductive atomic force microscopy (CAFM) to map the topographical structure of polycrystalline hafnia, and to examine the conductive properties of the dielectric. They manufactured an HfO<sub>2</sub> film with a nominal thickness of 5 nm using atomic layer deposition on a 1 nm thick interface layer of SiO<sub>2</sub> produced by oxidation on a silicon substrate. The hafnia layer was then annealed at 1000°C to induce crystallization.

The CAFM process uses a relatively thin electric probe to resolve nanometer-level structure of materials. The probe had a silicon tip, either uncoated or coated with a layer of conductive material. The process was performed both in air and in ultra-high vacuum (10<sup>-10</sup> mbar). The results showed a granular

structure of the dielectric, with grain boundaries (GB) having an average depth of  $\sim 1.6 \pm 0.4$  nm below the level of the grains.

Electrical conductance was examined using a  $-6.5$  volt bias, with the CAFM tip grounded and electrons injected into the silicon substrate. Analysis of the  $\sim 50$  grain boundaries showed an average width of  $\sim 4$  nm. The current map showed a correlation with the topographic map, confirming that the leakage conduction occurs primarily at the GB's. Breakdown (BD) spots were also identified, with diameters of  $\sim 20$  nm. The larger diameters indicated that the BD spots spread outside of the GB leakage sites into the grains. Further analysis indicated that the BD tends to propagate along with the GB's.

[Pirrotta et al. \(2013\)](#) also reported the use of CAFM to investigate the role of grains and GB's in conduction through polycrystalline hafnia. Their analysis confirmed that the leakage current flows primarily through the GB's.

The hafnia samples were produced by the same method and to the same specifications as in the experiment by [Iglesias et al. \(2011\)](#). They found that the average diameter of the grains was  $\sim 15$  nm, but with substantial variation. The measured leakage currents at GB's were found to be at least an order of magnitude higher than that at the grains. It was also found that  $\sim 5\%$  of the total area of the dielectric consisted of GB's.

A simulation study was also conducted, using the results of the CAFM analysis. The density of defects at grains was estimated to be  $3 \times 10^{19}$  cm $^{-3}$ . The defect density at GB's was estimated to be  $0.9 \times 10^{21}$  cm $^{-3}$  for a 3 nm HfO<sub>2</sub> thickness, and  $2.1 \times 10^{21}$  cm $^{-3}$  for a 5 nm HfO<sub>2</sub> thickness. Thus, the defect density was estimated to be more than an order of magnitude greater at the GB's than at the grains.

A more recent study ([Zhang et al., 2019](#)) examined the temperature dependence of the creation of a hafnia thin-film on a silicon substrate. Remote plasma atomic layer deposition was used at a temperature of 250°C to deposit a thin film of amorphous hafnia on the substrate for a number of specimens. Rapid thermal annealing was then used at various temperatures (450°C, 500°C, 550°C, and 600°C). The structural changes and crystallization properties of the hafnia thin films were then examined using atomic force microscopy, grazing incident X-ray diffraction, X-ray photoelectron spectroscopy, and high-resolution transmission electron microscopy. The temperature dependence of evolution of the HfO<sub>2</sub>/Si interface layer was also examined.

It was found that both the structure and the electrical properties of the dielectric were modified by annealing. At higher annealing temperatures, CAFM showed that, in agreement with the previous studies, the surface of the hafnia layer became more irregular. The grains grew, and the crevasses between grains became deeper. Before annealing, the hafnia was an amorphous layer on the silicon substrate. During annealing, however, the hafnia became polycrystalline, and a SiO<sub>2</sub> layer grew between the substrate and the hafnia. It was inferred that oxygen atoms from the hafnia diffused toward, and reacted with, the silicon. In the process, at higher annealing temperatures, the SiO<sub>2</sub> interface layer became monocrystalline. The hafnia layer's structure gradually evolved from amorphous through a monoclinic polycrystalline phase to an orthorhombic polycrystalline

phase (In a monoclinic crystal, the lattice is described by three vectors, forming a rectangular prism with a parallelogram as its base; in an orthorhombic crystal, the vectors form a rectangular prism, with all three vectors intersect at right angles (Kittel, 2004)).

The dielectric constant of the hafnia was also affected by annealing, at first increasing to a maximum of 17.2 at an annealing temperature of 500°C, then decreasing as the temperature approached 600°C. The authors concluded that an annealing temperature of 500°C produced the best results. At that temperature, there was a thin monocrystalline layer of SiO<sub>2</sub> atop the silicon substrate. Above that layer was another thin layer consisting of a combination of amorphous SiO<sub>2</sub> and amorphous hafnia, and above that layer was a layer of monoclinic polycrystalline hafnia. In monoclinic crystalline hafnia, the lattice unit is approximately cubic, described by three lattice vectors,  $\vec{a}$ ,  $\vec{b}$ , and  $\vec{c}$ . It has been found (Perevalov et al., 2007) that:

1.  $\|\vec{a}\| \cong 0.5106 \text{ nm}$ ,  $\|\vec{b}\| \cong 0.5165 \text{ nm}$ ,  $\|\vec{c}\| \cong 0.5281 \text{ nm}$ ,
2.  $\vec{a} \perp \vec{b}$ , and
3.  $\angle(\vec{a}, \vec{c}) = \angle(\vec{b}, \vec{c}) \cong 99.35^\circ$ .

Within the lattice unit, there are four hafnium ions and eight oxygen ions.

In summary, these studies showed the importance of the GB's for leakage current and for dielectric breakdown, with currents preferentially being channeled along with the GB's, rather than through the grains. Since approximately 5% of the volume of the hafnia consists of the GB's, there is a relatively small fraction of the dielectric that accounts for leakage current and breakdown current. When a breakdown occurs, it happens at the GB's, but a breakdown path spreads from the boundary into the surrounding grains, although the spread tends to be greater along with the GB's.

### 3.3. Mechanisms of Conduction Through Dielectrics

At absolute 0°K in a dielectric material, the valence band will be completely filled, and the conduction band empty. No current will flow under the influence of an electric field. At non-zero temperatures, there is a non-zero, small probability that an electron will be thermally excited across the band gap into a state in the conduction band. If so, then an applied electric field across the dielectric will induce a current. However, the current through the dielectric for usual applied electric fields will be very low. For large electric fields, there will be noticeable current due to various mechanisms (Chu, 2014). The observed mechanisms will depend on, among other factors, the configuration of the electronic component. It could be either an a) dielectric sandwiched between two metal plates, a MIM component, or b) dielectric sandwiched between a metal plate and a semiconductor, an MIS component. The observed conduction mechanisms will differ somewhat for the two types of devices. The conduction mechanism is discussed below.

Some of the conduction mechanisms depend on the properties of the electrode-dielectric contact and are called electrode-limited mechanisms. They include i) Schottky or thermionic emission, ii) Fowler-Nordheim tunneling, iii) direct tunneling, and iv) thermionic-field emission.

Other mechanisms, called bulk-limited mechanisms, depending on the properties of the dielectric itself. These are i) Poole-Frenkel emission, ii) hopping conduction, iii) ohmic conduction, iv) space-charge-limited conduction, v) ionic conduction, and vi) grain-boundary-limited conduction (in polycrystalline dielectrics).

### 3.3.1. Electrode-Limited Conduction Mechanisms

a) *Schottky or Thermionic Emission*: Schottky emission is a mechanism by which, if electrons in the metal obtain enough energy through thermal excitation, they will be able to overcome the energy barrier at the interface and enter the dielectric. In this mechanism, the current density is an increasing function of temperature. In the absence of an electric field across the dielectric, the emission current density is given by

$$J_{Sc} = A^* T^2 e^{-W/kT}.$$

Here,  $W$  is the work function, the minimum thermal energy needed for an electron to escape the surface of the cathode and enter the dielectric,  $k$  = Boltzmann's constant,  $T$  = Kelvin temperature, and

$$A^* = \frac{4\pi q k^2 m^*}{h^3},$$

where  $q$  = electron charge,  $h$  = Planck's constant, and  $m^*$  = effective electron mass in the dielectric<sup>1</sup>.

The work function,  $W = q\varphi_B$  is the Schottky barrier height at the surface. In the presence of an electric field,  $E$ , the work function is reduced by

$$\Delta W = \sqrt{\frac{q^3 E}{4\pi\epsilon_r\epsilon_0}}.$$

At  $T = 0^\circ K$ , the emission current density is 0. At an operating temperature of  $400^\circ K$  ( $260.31^\circ F$ ) and constant electric field stress of  $1 \text{ mV/cm}$ , the emission current density is approximately  $1\mu A/cm^2$ .

If there are traps and interface states in the dielectric, so that the electron mean free path,  $l$ , is smaller than the dielectric thickness,  $t_d$ , then the equation for the current density must be modified to

$$J_{Sc} = \alpha T^{1.5} E \mu \left( \frac{m^*}{m_0} \right)^{1.5} e^{-\frac{W-\Delta W}{kT}},$$

---

<sup>1</sup>  $\frac{1}{m^*} = \frac{1}{\hbar^2} \frac{\partial^2 E}{\partial k^2}$ ,  $p = \hbar k$  = electron momentum,  $E$  = electron energy

where  $m_0$  = free electron mass and  $\alpha = 3 \times 10^{-4} \frac{A - sec.}{cm^3 k^{1/5}}$ . In this case, the temperature dependence of the emission current density is somewhat reduced.

The electron mobility in the dielectric is denoted by  $\mu$ . In a vacuum, if there is an electric field, a charge carrier, such as an electron, will be accelerated in the direction opposite the electric field. However, in a dielectric, collisions between electrons and the atoms or molecules of the dielectric will lead to an average constant electron velocity opposite the direction of the field. The electron mobility is the constant of proportionality between this average velocity and the field strength.

b) *Fowler-Nordheim Tunneling*: This process occurs when the applied electric field across the dielectric is large enough to induce a triangular interface potential barrier between the metal and the dielectric. This mechanism is independent of temperature; it depends on the electric field strength and the surface barrier height. The equation for the current density is

$$J_{FN} = \frac{q^3 E^2}{8\pi h^3 q \varphi_B} \exp \left[ \frac{-8\pi \sqrt{2qm_T^*}}{3hE} \varphi_B^{1.5} \right],$$

where  $m_T^*$  is the tunneling effective mass of the electron in the dielectric. If the dielectric thickness is large enough (for example, greater than about 4 nm in  $SiO_2$ , the tunneling effective mass is approximately the same as the effective mass of the electron in the dielectric,  $m^*$ .

At low voltage stress, the thermionic emission current is negligible, and this tunneling current is dominant. As the electric field strength increases, the Fowler-Nordheim tunneling current density increases.

c) *Direct Tunneling*: For lower applied electric fields, direct tunneling can occur across the dielectric. In this case, the tunneling occurs across the full dielectric thickness. This type of current would of course be smaller than Fowler-Nordheim tunneling current. Again, this mechanism is independent of temperature but does depend on the dielectric thickness, being smaller for thicker dielectrics. The direct tunneling current density is given approximately by:

$$J_{Tun} \cong \exp \left\{ -\frac{8\pi \sqrt{2q}}{3h} (m^* \varphi_B)^{0.5} \kappa t_{EOT} \right\}.$$

Here,  $t_{EOT} = t \left( \frac{\kappa_{SiO_2}}{\kappa} \right)$  is the equivalent oxide thickness of the dielectric,  $\kappa$  is the dielectric constant of the dielectric, and  $\kappa_{SiO_2}$  is the dielectric constant of silicon dioxide. Obviously, if the dielectric is silicon dioxide, then  $t_{EOT} = t$ .

Note that the direct tunneling current density is (approximately) independent of the voltage stress. At low temperatures and low applied voltage, direct tunneling is the dominant mode of conduction and is a decreasing function of dielectric thickness.

d) *Thermionic Field Emission*: This mechanism is intermediate between Schotky emission and F-N tunneling. The electrons gain some energy by thermal excitation so that they “see” an even smaller triangular potential barrier and

are able to tunnel through more easily. This mechanism is, of course, temperature dependent. The current density is given by

$$J_{TF} = \frac{q^2 \sqrt{mkT} E}{2h^2 \pi^{0.5}} \exp\left(-\frac{q\varphi_B}{kT}\right) \exp\left(\frac{h^2 q^2 E^2}{96\pi^2 m (kT)^3}\right).$$

This conduction mechanism is mildly dependent on the temperature and strongly dependent on the electric field across the dielectric.

### 3.3.2. Bulk-Limited Conduction Mechanisms

e) *Poole-Frenkel Emission*: This type of conduction occurs when electrons in trapping sites gain enough energy through thermal excitation to jump out of the trap into the conduction band of the dielectric. This type of emission is more likely to occur if an electric field is applied across the dielectric, thus reducing the potential energy of the trapped electron. The current density is given by

$$J_{PF} = q\mu N_C E \exp\left[\frac{-q(\varphi_T - \sqrt{\frac{qE}{\pi\epsilon_i\epsilon_0}})}{kT}\right].$$

Here,  $N_C$  is the density of states in the conduction band of the dielectric, and  $\varphi_T$  is the trap energy level. This current density will be larger for the larger density of available states in the conduction band and with a larger applied electric field (thus increasing the available energy to be absorbed by a trapped electron). It is a decreasing function, however, of the trap potential – the larger the gap between the trap and the conduction band, the smaller the current density.

Poole-Frenkel emission has been observed to be the dominant conduction mechanism in certain dielectric materials when there is a combination of high electric fields ( $> 1$  mV/cm) and for temperatures between 300°K and 400°K.

f) *Hopping Conduction*: This conduction occurs when an electron in a trapping site is able to tunnel from one trap to another. If there is a complete sequence of trapping sites across the dielectric (a percolation path), the electron may tunnel from trap to trap across to the anode. The current density is

$$J_{Hop} = qan\nu \exp\left[\frac{qaE}{kT} - \frac{E_a}{kT}\right],$$

where  $a$  is the mean hopping distance from one trap to the next,  $n$  is the electron concentration in the conduction band of the dielectric,  $\nu$  is the frequency of thermal vibration of electrons at trap sites, and  $E_a$  is the activation energy, the energy level from the trap states to the bottom of the conduction band. This mechanism differs from Poole-Frenkel emission in that the electrons are not thermally excited into the conduction band, but tunnel from one trap site to another.

g) *Ohmic conduction*: This occurs when there are electrons in the conduction band of the dielectric and holes in the valence band. A hole is a vacant state in the valence band, which acts effectively as a positive charge that can conduct current, although a hole current moves in the opposite direction than a current of electrons. This conduction mechanism is somewhat temperature dependent. Its current density is

$$J_{Ohm} = \sigma E = q\mu EN_C \exp\left(\frac{-E_g}{2kT}\right),$$

where  $\sigma$  is the electrical conductivity,  $\mu$  is the electron mobility,  $N_C$  is the effectivity density of states in the conduction band, and  $E_g$  is the band gap (the difference between the top state in the valence band and the lowest state in the conduction band). The magnitude of the Ohmic current is very small until the dielectric breakdown.

h) *Space-Charge-Limited Conduction*: This mechanism is caused by the injection of electrons into the dielectric at an ohmic (metallic) contact. The electrons diffuse through the dielectric toward the anode under the influence of the electric field. If the electrons were injected into a vacuum instead of into the dielectric (as in a vacuum tube device), they would accelerate toward the anode. Since there is a solid (the dielectric material) between the cathode and anode, the injected electrons experience collisions with the lattice sites, leading to diffusion across the dielectric with a constant average velocity. If there are trapping sites in the dielectric, the space-charge limited conduction current density is given by

$$J_{SCL} = \frac{9}{8}\mu\epsilon \frac{N_C}{g_n N_t} \exp\left(\frac{E_t - E_C}{kT}\right) \frac{E^2}{d},$$

where  $g_n$  is the degeneracy of energy states in the conduction band,  $N_t$  is the density of traps in the dielectric,  $E_t$  is the trap energy level (assumed to be single-valued),  $E_C$  is the lowest energy level in the conduction band, and  $\epsilon$  is the static dielectric constant. The other quantities are as defined previously.

In the case of very strong injection of electrons into the dielectric (a strong potential difference, approaching breakdown), all traps are filled with electrons, and the space-charge limited conduction current density follows Child's law:

$$J_{Child} = \frac{9}{8}\mu\epsilon \frac{E^2}{d}.$$

This current density has a square-voltage dependence, since  $V = E/d$  for a constant electric field across the dielectric.

j) *Ionic Conduction*: This occurs when ions move due to an applied electric field. For example, if there are defects or impurities in the dielectric film, the field may cause ions to jump from one defect site to another. The current density is

$$J_{Ion} = J_0 \exp\left[-\left(\frac{q\varphi_B}{kT} - \frac{Eqd}{2kT}\right)\right],$$

where  $J_0$  is a proportionality constant and  $d$  is the spacing of two nearby jumping sites. Since ion masses are relatively large, this mechanism is not usually significant in dielectric films in CMOS applications.

k) *Grain-Boundary-Limited Conduction*: In a polycrystalline dielectric, resistivity at boundaries between microcrystals may be higher than that within the microcrystals. At the grain boundary, there will be a potential energy barrier which is proportional to the square of the trap density at the boundary and inversely proportional to the relative dielectric permittivity of the dielectric:

$$\Phi_B = \frac{q^2 n_b^2}{2\epsilon N},$$

where  $\epsilon$  is the relative permittivity,  $n_b$  is the trap density at the boundary, and  $N$  is the dopant concentration. The greater the trap density at the boundary, the larger the potential barrier; the greater the relative permittivity, the lower the potential barrier.

In hafnia, this type of conduction is important, since empirical evidence given above shows that leakage current and breakdown current are both preferentially channeled along the grain boundaries.

### 3.4. Breakdown in Silicon Dioxide Dielectrics

In thick dielectrics, it is unlikely that there will be quantum tunneling of electrons from the cathode to the anode. However, in thin film dielectrics, with thicknesses of the order of several nanometers, tunneling probabilities are larger. Prior to the formation of a complete percolation path across the dielectric, tunneling is the primary means of current flow between the cathode and the anode.

Once a complete percolation path is formed, electrons can also jump from trap to trap due to thermal excitation. In this manner, they pass from cathode to anode. In addition, an electron in a trapping site is closer to the anode than an electron at the cathode and thus has a higher probability of tunneling from the site across to the anode. This sudden increase in conduction through the dielectric is called soft breakdown. There may be several soft breakdown occurrences before the final failure of the dielectric.

Consider a capacitor consisting of two metal plates with a thin film of  $\text{SiO}_2$  dielectric sandwiched between them. Let the area of the plates (and the dielectric) be  $A$ . Let the capacitor be subjected to a voltage stress, either constant or time-varying. Prior to the formation of a complete percolation path, at reference time  $t = 0$ , tunneling is the only means of current flow, as represented by the equation

$$AJ_{\text{stress}} = AJ_{\text{Tun}},$$

where the tunneling current density is a decreasing function of the dielectric thickness,  $T_{ox}$ , but an increasing function of the applied voltage  $V(t)$ :

$$J_{\text{Tun}} = \alpha t_{\text{EOT}} e^{-\beta t_{\text{EOT}}/V(t)}.$$

Once a complete percolation path has been formed, additional current begins to flow, and the current equation becomes

$$AJ_{\text{stress}} = AJ_{\text{Tun}} + AJ_{\text{disp}} + \{I_{\text{perc}}\}.$$

Here,

- a)  $J_{\text{disp}} = \frac{\varepsilon}{t_{\text{EOT}}} \frac{dV}{dt}$  is called the displacement current, and  $\varepsilon$  is the dielectric permittivity. This current is due to time variation in the electric dipole moments of the  $\text{SiO}_2$  (and silanol and water) molecules. If the voltage stress across the dielectric is constant, there is no displacement current.
- b)  $\{I_{\text{perc}}\} = \{G_0(t)\} V(t)^\delta$  is the percolation current, or hopping across a complete path. It is area-dependent and sample-specific. Each sample has a different time-dependent conductance,  $\{G_0(t)\}$ , which also depends on the density of trapping sites in the dielectric (and so on the particulars of the deposition process) and on the power being dissipated by the percolation current (this dependency is denoted by the braces around the conductance and the current). The exponent of the voltage is found empirically ([Alam, Weir and Silverman, 2002](#)) to be less than 1.

It is clear that each current density term in the previous equation contains more than one of the conduction mechanisms described in the previous section. For example, the tunneling current density term includes, not only direct tunneling but also Fowler-Nordheim tunneling, which also depends on the electric field strength. This phase will also include low levels of conduction due to the various temperature-dependent mechanisms. The percolation current density includes several conduction mechanisms, with dependency on field strength, temperature, electron concentration in the conduction band of the dielectric, mean hopping distance from one trap to another, etc. Hopping, or trap-assisted tunneling (TAT), would appear to be the dominant conduction mechanism during this phase until the local temperature at the percolation path becomes large enough to trigger hard breakdown and the ohmic conduction phase.

As percolation current flows across the dielectric, power is dissipated through the percolation path  $P_{\text{perc}}(t > 0) = V(t > 0)I_{\text{perc}}(t > 0)$ . If this power dissipation is large enough, the local temperature will be high enough near the percolation path to melt silicon, leading to a short-circuit through the dielectric. In addition, the increase in temperature due to the percolation current may locally increase the current flow due to the temperature-dependent mechanisms discussed above. There is thus a feedback mechanism; as the percolation current increases the local temperature, thus increasing the currents due to other mechanisms, the temperature increases further. The current following this short-circuit is found empirically ([Alam, Weir and Silverman, 2002](#)) to be proportional to the voltage stress, thus obeying Ohm's law. The result is called a hard breakdown of the dielectric, as the dielectric becomes a resistor.

### 3.5. Breakdown in Hafnium Oxide Dielectrics

In a hafnium oxide thin film dielectric with a silicon dioxide interface layer, the breakdown mechanism is similar to that of a silicon dioxide thin film, but also different in some ways. In the dielectric specimens described in the most recent study (Zhang et al., 2019), there is a monocrystalline  $\text{SiO}_2$  layer atop the silicon substrate, then a thin mixed layer of amorphous  $\text{SiO}_2$  and amorphous hafnia atop that, and a thicker layer of monocline polycrystalline hafnia above that.

Electrons emitted by the silicon substrate cathode may cross the monocrystalline  $\text{SiO}_2$  layer by various methods discussed above, particularly through direct tunneling and Fowler-Nordheim tunneling (Perevalov et al., 2007). When they reach the amorphous layer of  $\text{SiO}_2$  and hafnia, they encounter a potential barrier, due to the larger concentration of defects in this layer. They are then channeled along with this layer until reaching a grain boundary of the polycrystalline hafnia layer. They may then hop from trap to trap in this grain boundary to reach the anode. It is unlikely that leakage will cross the grains since the defects (elongated hafnium–oxygen bonds) are much more concentrated in the GB's. This means that roughly 5% of the volume of hafnia primarily accounts for current flow.

As electrons hop from trap to trap in the grain boundary, the local varying electric field which they produce generates phonons<sup>2</sup> in the adjacent grains Vandelli et al. (2013), increasing the local temperature. The vibrations also tend to generate more oxygen vacancies (trapping sites) in the grain boundary, increasing the trap density. The increased temperature also enhances the various temperature-dependent conduction mechanisms, leading to increasing leakage current. The increased trap density leads to increased trap-assisted tunneling, as the distance between adjacent trapping sites is smaller. The increased leakage current, in turn, leads to the generation of more trapping sites and higher local temperature.

If the damage is relatively small, and the local percolation path is primarily confined to the GB, then the capacitor may discharge as a soft breakdown event, with the subsequent buildup of charge due to the continuing voltage stress (Chatterjee et al., 2006). If, however, the temperature-induced damage is significant, then the positive feedback leads to a runaway leakage current melts an ohmic conduction path along the grain boundary, producing hard dielectric breakdown. There will be a primary, initial grain boundary ohmic conduction channel, but there may also be secondary channels through the dielectric. There may be several SB events prior to the HB event. After HB, the capacitor is converted into a resistor, with the resistance dependent on the details of the channels of ohmic conduction.

## 4. Cell Models for Dielectrics

Le, Bažant and Bazant (2009), Le (2012) and Bažant and Le (2017) (Chap-

---

<sup>2</sup>A phonon is a quasiparticle of sound in a crystal lattice; it is quantized due to the regularity of the lattice structure.

ter 14) proposed a subcell model for high-gate dielectrics. Here, the dielectric is viewed as a parallel circuit of cells and where each cell is a series circuit of nano-capacitors subcells. Because it is a parallel circuit, each cell (also referred to as a *representative volume element (RVE)* by [Bažant and Le \(2017\)](#)) is a bundle load-sharing system where the capacitor laws dictate the load on each working subcell. As such, the dielectric is a chain-of-bundles load-sharing reliability system where the system fails when one of the bundles/cells fails.

Other cell-type of models have been considered earlier to analyze the BD of a dielectric but these are defect based rather than based on load-sharing. See [Strong et al. \(2009\)](#) Section 3.2–3.4 where percolation and analytic cell models are discussed in detail.

The cells in the analytic model are akin to the subcells in [Le, Bažant and Bazant \(2009\)](#)'s model without regard to load-sharing and are considered defective cells if they contain a defect. Cells being defective are independent Bernoulli random variables where the probability of being defective is  $\lambda$ , the mean fraction of defective cells in the dielectric. The dielectric fails when there is a collection of defective cells that go directly across the thickness of the dielectric since this causes current to flow across the dielectric.

In the percolation model, which is the more appropriate model for thin-film silicon dioxide dielectrics, defects are impurity sites in the amorphous material. Most of the sites in the material consist of silicon dioxide molecules bound within the dielectric. However, as discussed in the previous section, the manufacture of the thin film leads to the inclusion of impurity sites, consisting of either silicon hydroxide (silanol) or water. A hydrogen ion (proton) in a defect site may, under the influence of an electric field across the dielectric, exchange positions with an adjacent oxide ion in a silicon dioxide site. In this way, the impurity site, which acts as an electron trap, may migrate through the dielectric. If it happens that the various migrating traps temporarily form a chain (percolation path) of adjacent traps extending across the dielectric, then there will be a temporary increase in the leakage current, a soft breakdown (SBD), which will also lead to an increase in the local temperature around the chain of traps. However, the continued migration of the trapping sites will lead to dispersal of the percolation path. Another percolation path may form later at a different place in the dielectric. If it happens that the SBD current in a path leads to a sufficient increase in the local temperature to produce melting of an ohmic conduction path through the dielectric, then hard breakdown (HBD) is said to occur.

In a thin-film hafnium oxide dielectric, on the other hand, the percolation model does not work so well. The trapping sites do not migrate through the dielectric but are confined largely to the grain boundaries (GBs). Leakage current flows across the dielectric almost exclusively at the GBs. The leakage current through a GB increases the local temperature, leading to the generation of more dislocations (trapping sites) in the GB. The consequence is a temporary increase in leakage current (SBD), with concurrent capacitor discharge. However, the traps do not migrate through the dielectric but remain localized in the GB. Repeated SBD events at a GB may lead to a sufficient increase in the local

temperature to begin generating dislocations (traps) in the grains adjacent to the GB, producing a permanent conductive path across the dielectric, a hard breakdown.

The cell model is more appropriate for thin-film hafnium oxide dielectrics, because of the localization of the paths for SBDs and HBDs. Each cell may be conceptually considered to be a series of SBD events, leading to an HBD. The cells are parallel, due to localization. A series of pseudo-nanocapacitors in a cell, for which sequential subcell failure leads to cell failure and HBD, may approximate the sequence of SBDs leading to HBD. Each SBD event increases the local temperature at the GB, increasing the probability of future SBDs at that location, and of the eventual HBD.

The above models are related to *chains-of-links* (bundles) types of models where the chain fails when one of the links fails (the *weakest link model*). The number of links is determined by the size (cross-sectional area) of the links and the number of cells/subcells in a link is determined by the size of the cell and the thickness of the dielectric. If the cells/elements in the links are independent and identically distributed (i.i.d.), extreme value asymptotics suggest that the BD statistics would be approximately Weibull for long chains. Lack of fit of the Weibull is attributed to size effects of the finite length of the chain where [Le \(2012\)](#) and [Bažant and Le \(2017\)](#) referred to the model as a *finite weakest link* model.

Though they based their model on a bundle/cell being a series circuit of nano-capacitors, this is just an approximate model that is not consistent with the nano-physics of BD as indicated in the previous section. Rather than using their load-sharing cell model to study the size effect related to [Kim and Lee \(2004\)](#)'s Figure 14 data and to correct for this inconsistency, they empirically fit what they call a *grafted distribution* for the BD cycle time. The grafted distribution behaves like a Weibull at the origin and like a normal distribution in the right tail and serves as a reference distribution to the size effect.

Size effects were observed earlier in the study of the BD of fibrous composites ([Phoenix, 1983](#); [Phoenix and Tierney, 1983](#); [Taylor, 1987](#)). They modeled composites as chains-of-(load-sharing) bundles where size effects need to be addressed in the analysis of the chains. They used a reference distribution to discover the length,  $m$ , of the chain and the size,  $n$ , of the bundle. (See the discussions regarding the “weakest link transform” and the “reverse weakest link relationship” in Section 6 of [Phoenix and Tierney \(1983\)](#), and Section 5 of [Taylor \(1987\)](#), respectively.) Their way of selecting the bundle size (the RVE) depended on the bundles being approximately i.i.d..

In Section 10 we study the size effects of a finite weakest-link/chain-of-bundles model for [Kim and Lee \(2004\)](#)'s Figure 14. Our study is based on a hybrid of [Le, Bažant and Bazant \(2009\)](#)'s model and the fibrous composite model which are both chain-of-bundles load-sharing systems. In the hybrid, we just choose a reference distribution without regard to the details of the statistical behavior of the elements of the bundle which is quite complicated to model for complicated materials. The reference distribution is simply based on load-sharing bundles of  $n$  i.i.d. Weibull components where the load-sharing within the bundle is the

equal load-sharing rule.

The Weibull parameters and  $n$  are tuning parameters to study the size effect of the chain length and the bundle size that can be used to incorporate the physical structure of the dielectric. Note that the relationship of the Weibull shape parameter,  $\beta$ , in the asymptotic distribution of the TBD statistic under static testing protocols is  $\beta \cong T_{ox}/a_0$ . Here,  $T_{ox}$  is the thickness of the  $\text{HfO}_2$  dielectric and  $a_0$  is the lattice constant for the grain. (See formula (3.17) of [Strong et al. \(2009\)](#) where, here, we ignore the thickness of the interface since it is negligible for more modern fabrications of  $\text{HfO}_2$  dielectrics.)

We also consider the fabrication of the  $\text{HfO}_2$  dielectrics where the conductive region of the grain boundaries is where the BD of the dielectric occurs since the crystalline structure of the grains makes it magnitudes more difficult for electrons to move through/jump around in the grain until the behavior of the electrons becomes irreversible. As indicated in the previous section, electrons in the cathode end traverse the interface with the  $\text{HfO}_2$  dielectric laterally until it reaches a grain boundary that it is physically capable of entering. The electrons attempt to move across to the anode through the grain boundaries described in the previous section. Thus, the length of the chain,  $m$ , is dictated not by the total cross-sectional area but just that consisting of the grain boundaries. Finally, another consideration we discuss, is how the topography of the  $\text{HfO}_2$  surface at the anode end can be incorporated into the model.

## 5. Part II Introduction: Statistical Aspects

The basic model for BD is the chain-of-bundles model. This is a weakest link model for materials where the chain/material fails when one of its bundles/links fail. [Rosen \(1964, 1965\)](#) used such a model in the analysis of his seminal experiments regarding unidirectional 2-D glass fibers composites. He discovered that around a break in a fiber in the composite all the load was transferred to fibers horizontally in the composite. He referred to this horizontal distance as the ineffective length and used this to conceive of the composite as a chain-of-bundles where each bundle was a horizontal collection of ineffective length fibers.

Following [Daniels \(1945\)](#)'s work on the breaking strength of a bundle of threads, [Rosen \(1964, 1965\)](#) used the equal load sharing rule among the surviving fiber elements in a bundle. This rule, though reasonable for a bundle of threads or a dry bundle of fibers, was unrealistic for fibrous composites. [Zweben and Rosen \(1970\)](#) used more realistic local load-sharing rules for 3-D composites.

Rosen's work initiated a considerable amount of work on chain-of-bundles load-sharing systems for fibrous composites in 1970's and 1980's. Notable was the work by a group of material scientists and statisticians at Cornell (see, for example, [Harlow and Phoenix \(1978a,b, 1982\)](#); [Harlow, Smith and Taylor \(1983\)](#), and the references cited in Section 4).

In Section 6, electrical break down (BD) and the BD formalism that relate various types of breakdown distributions is discussed while in Section 7 the statistical properties of the load-sharing bundles and chains of such bundles are

presented. A mixture representation is given for the bundle breaking strength distribution when the bundle component strength distributions are i.i.d.. The shape parameter depends on the bundle size and the scale parameter is determined by the load-sharing rule in this representation. The Gibbs measure for the set of surviving components is also given and a description of the stochastic process for electrical BD is given that is consistent with the BD of a series circuit as a load-sharing system and the distribution of the BD of the stochastic process.

[Kim and Lee \(2004\)](#) did a thorough study of reliability characteristics of the BD of  $\text{HfO}_2$  dielectrics. Statistical analyses of their data for Figures 3, 6, and 14 regarding the BD formalism are given in Section 8. (The data for Figure 14 was kindly provided by [Le \(2012\)](#) who used this data in his analysis of his load-sharing cell model. The data from Figures 3 and 6 were reconstructed from the figures since J. C. Lee was not successful in locating this data.)

In Section 9, the analysis of [Kim and Lee \(2004\)](#)'s Figure 6 is used to study the BD of circuits of ordinary capacitors. This is for illustrative purposes only to illustrate size effects since the capacitor BD is based on dielectrics and not classical plate capacitors. We also study parallel/series circuits (chain-of-bundles) to study simulation size effects as well the size effect of the chain length. We also discuss the load-sharing aspects that have to be considered in time to BD and cycles to BD.

[Le \(2012\)](#) and [Bažant and Le \(2017\)](#) discussed the size effect of the length of the chain in the chain-of-cells/bundles model and refer to this as the finite weakest link model. We study this in Section 10 and suggest hybrids of their load-sharing cell model that is described in Section 4 with earlier work by [Phoenix \(1983\)](#); [Phoenix and Tierney \(1983\)](#); [Taylor \(1987\)](#) who studied methods for discovering the length of a chain and the size of a bundle. These hybrids suggest how (i) one may account for the coarseness in the metal anode interface with the  $\text{HfO}_2$  surface and (ii) a birth process akin to [Taylor \(1987\)](#)'s model to account for the creation of an ohmic path that causes BD in the dielectric.

A summary of the paper is given in the last section on concluding comments.

## 6. Electrical Breakdown (BD) and the BD Formalism

In the testing of capacitors and capacitor circuits, one is interested in their reliability. Thus, one studies various types of breakdown under accelerated stress conditions: e.g., stressed under increasing voltage or current to determine voltage or current breakdown (VBD or CBD) and time to failure under static voltage or current load or cycles to failure. The BD formalism allows one to relate BD under different testing protocols and to project the reliability to normal operating conditions.

### 6.1. The BD Formalism

Fundamental to the understanding of *electrical breakdown* of plate capacitors is a formalism based on the Weibull distribution. Much of the justification for the

use of the Weibull is empirically based and motivated by weakest link arguments. In particular, [Kim and Lee \(2004\)](#) used Weibull plots in Figures 6, 3 & 8 and 14 and information in these figures to study the BD statistics of metal oxide ( $\text{HfO}_2$ ) capacitors under these three protocols.

Next, we present the necessary background regarding this formalism for static and dynamic loads. This is based on Chapters 2 and 3 from [Strong et al. \(2009\)](#) and Chapters 14–17 from [Dissado and Fothergill \(1992/2008\)](#). See also [Phoenix \(1983\)](#) and [Phoenix and Tierney \(1983\)](#) who gave a more general formalism in a different format for composites that includes general load history in BD and derived the power law from first principles.

## 6.2. Time to BD (TBD) Formalism: Static Loads

In this subsection, we present the assumptions/axioms A.1–3 and their consequences of the formalism for static loads.

**A.1 Weakest Link Principle:** Let  $F_A$  denote the TBD distribution of a plate capacitor with area  $A$ . Then,

$$1 - F_A = (1 - F_1)^A,$$

where  $F_1$  is the TBD distribution of a plate capacitor of unit area. Note that it follows from this that

$$1 - F_{A+B} = (1 - F_1)^{A+B}.$$

So, the voltage BD statistics for two disjoint areas are independent.

**A.2 Weibull Distribution for the time to BD,  $T$ , under a static voltage load,  $V$ , and unit gate area ( $A = 1$ ):**

$$\text{Survival Function: } S(t) \equiv S(t; \tau, V, a) = \exp \left\{ - \left( \frac{t}{\tau(V)} \right)^a \right\};$$

$$\text{Hazard Function: } h(t) = a\tau(V)^{-a}t^{a-1}.$$

**A.3 The Inverse Power Law Relationship of the Parameters of  $T$  to that of  $V$ :**

$$\tau(V) = DV^{-n} \equiv C^{-1/a}V^{-b/a}.$$

**Consequences of A.2 & A.3:** (i) The scale parameter,  $\tau(V)$ , the characteristic lifetime, is the  $1 - e^{-1}$  percentile of  $T$  under a static load  $V$ . Let  $t_p(V)$  and  $\mu(V)$  denote the  $p$ th percentile and mean of  $T$  under a static load  $V$ . Then, since

$$[t_p(V)]^a = [\tau(V)]^a [-\ln(1 - p)] \text{ and } \mu(V) = \tau(V) \int_0^\infty at^a e^{-t^a} dt,$$

it follows that the percentiles and the mean of the time to BD also satisfies the inverse power law. The shape parameter,  $a$ , is related to the thickness of the

capacitor (see Section 3.2.5 of [Strong et al., 2009](#)).

(ii) Since

$$\ln \tau(V) = -n \ln V + \ln D,$$

plots of  $\ln \tau(V)$ ,  $\ln \mu(V)$  and  $\ln t_p(V)$ ,  $p = 0.5$ , versus  $\ln V$  are used to verify the appropriateness of the inverse power law model. For example, see Figure 14.7 from [Bažant and Le \(2017\)](#), Figure 3.43b from [Strong et al. \(2009\)](#) and Figures 14.8b and 14.5a from [Dissado and Fothergill \(1992/2008\)](#)), respectively. Note that the related Figures 3.43a and Figure 14.5b suggest that the exponential law is a reasonable alternative to the inverse power law for those figures.

Section 14.2.1 of [Dissado and Fothergill \(1992/2008\)](#) compared the inverse power and exponential laws and indicate why the inverse power law is preferred. Section 3.4.1 of [Strong et al. \(2009\)](#) discussed in-depth the deficiencies of the exponential law and stated on page 271–2 that “At lower voltages or for thinner oxides, the TBD power law dependence remains valid over 12 orders of magnitude as seen in Figure 3.46(b). Recently, the empirical TBD power law was also confirmed by different groups. These independent studies from different research groups unambiguously demonstrate that an exponential law is invalid to characterize the TBD voltage dependence for both thin and thick oxides.” In addition, [Phoenix \(1983\)](#) page 227 and [Phoenix and Tierney \(1983\)](#) page 215 stated that “In summary, the notion that the exponential breakdown rule is theoretically justified from kinetic theory, and that the power-law is only an “empirical” law without foundation. Not only is the power-law theoretically justified, it also has the added advantage of mathematical tractability.”

**Consequences of A.1 & A.2:** At a fixed voltage  $V$  and gate area  $A$ , the characteristic lifetime,  $\tau(V, A)$ , is

$$\tau(V, A) = \tau(V) A^{1/a}.$$

It follows from Consequences of A.2 & A.3(i) how the  $p$ th percentile,  $t_p(V, A)$ , and mean,  $\mu(V, A)$ , also preserve this relationship. [Kim and Lee \(2004\)](#)’s Figures 8 and 9 are consistent with A.1 & A.2.

### 6.3. TBD Formalism: Dynamic Loads

Assumption A.1 for static loads is a special case of the proportional hazards model where the proportionality is proportional to the area. In our analysis of [Kim and Lee \(2004\)](#)’s Figure 6 data for increasing voltage load, in Section 8.2, we find that a proportional hazards model was appropriate but it was not proportional to the area. For dynamic loads, we replace A.1 by A.1’ but keep A.2 and A.3.

**A.1’ Weakest Link Principle:** Let  $F_A$  denote the TBD distribution of a plate capacitor with area  $A$ . Then,

$$1 - F_A = (1 - F_1)^{m(A)},$$

where  $F_1$  is the TBD distribution of a plate capacitor of unit area and  $m(A)$  is a nonnegative increasing function. Note that it follows from this that if  $A < C$  with  $C = A + B$ ,

$$\begin{aligned} 1 - F_C &= (1 - F_1)^{m(C)} = (1 - F_1)^{m(C) - m(A)}(1 - F_1)^{m(A)} \\ &= (1 - F_1)^{m(C) - m(B)}(1 - F_1)^{m(B)}. \end{aligned}$$

So, the voltage BD statistics for two disjoint areas are independent.

#### A.4 Time and Voltage Relationship for the Probability of Breakdown:

Plugging  $\tau(V) - C^{-1/a}V^{-b/a}$  from A.2 into the hazard rate in A.1 gives

$$h(t) = at^{a-1}CV^b \text{ or } h(t) = at^{a-1}C(V(t))^b$$

if the voltage is a function of  $t$ . When  $V(t) = Vt$ , then

$$h(t) = Cat^{a+b-1}V^b.$$

Thus, the *hazard function* of  $T$ ,

$$H(t) = \int_0^t h(s)ds = \int_0^t Cat^{a-1}[V(s)]^b ds = \begin{cases} Ct^aV^b, & \text{if } V(t) \equiv V, \\ C\frac{at^{a+b}V^b}{a+b}, & \text{if } V(t) \equiv Vt, \end{cases}$$

and the survival function is

$$S(t) = \exp\{H(t)\} = \begin{cases} \exp\{-Ct^aV^b\}, & \text{if } V(t) \equiv V, \\ \exp\left\{C\frac{at^{a+b}V^b}{a+b}\right\}, & \text{if } V(t) \equiv Vt. \end{cases} \quad (6.1)$$

Thus, from Eq. (6.1), under an increasing voltage, assumption A.2 and  $V(t) = Vt$ , the breakdown time,  $T_{BD}$ , has a Weibull distribution with shape parameter  $\rho$  and scale parameter (characteristic life)  $\tau$  where

$$\rho = a + b, \tau^{-1} = \left(Ca\frac{V^b}{a+b}\right)^{1/(a+b)} \text{ and } n = \frac{b}{a}. \quad (6.2)$$

**Remark:** Since  $V(t) = Vt$ , from Eq. (6.2) the BD voltage  $V_{BD} = VT_{BD}$ ,  $V_{BD}$ , has a Weibull distribution with shape parameter  $\rho$  and scale parameter (characteristic life)  $V\tau$ .

Similar assumptions to those above are relevant to cyclic testing. For example, for AC tests, the pulse voltage amplitude,  $V$ , will be constant for static testing while, for dynamic testing, the amplitude rate,  $V$ , is proportional to time. (See Formulas (16.28-29) and (17.5-7b) of [Dissado and Fothergill, 1992/2008](#)). The data for Figure 14 of [Kim and Lee \(2004\)](#) is for static cyclic testing with the added feature that each cycle has a duty cycle (an on cycle) when the capacitor is under static cyclic testing and an off-cycle when it is under no stress.

For the limited amount of data for Figure 14, [Kim and Lee \(2004\)](#) suggested that changes in the frequency and the length of the on-cycle seemed to only affect the scale but not the shape parameter. A statistical analysis of this is discussed in Sections 8.1 and 10 as well as the data from other figures in their paper.

## 7. Statistical Properties of a Load-Sharing Bundle

A series circuit of statistically independent capacitors fails when all of the capacitors fail. As such, it is a reliability parallel system, and, because of the electrical laws, it is a load-sharing reliability system. (As mentioned earlier, these are equilibrium rules since a capacitor failure can precipitate a cascade of failures that is not easy to model.) Such a load-sharing system is referred to as a **bundle**. Below we give the survival distribution and mixed distribution of the strength of a bundle under increasing load. After that, we give the joint distribution, the Gibbs measure, of the state (failed/working) of the components of a bundle and discuss the stochastic failure process for the bundle.

### 7.1. The Bundle Strength Distribution as an Affine Mixture

The strength of a load-sharing bundle is based on the nominal load per component (the load per component), say  $x$ . We assume that there are  $n$  components in the bundle  $N = \{1, 2, \dots, n\}$ . Let  $M \subseteq N$  denote the set of working component in  $N$ , then the load at component  $i \in M$  for a nominal load per component  $x$  is given by  $\lambda_i(M)x$ . These nonnegative constants,  $\lambda_i(M)$ , define the load sharing, and the collection  $\{\lambda_i(M) : i \in M, M \subseteq N\}$  is called a load-sharing rule.

Consider  $m$  sets of working components in the bundle  $N \supseteq S_1 \supset S_m \supset S_{m+1} = \emptyset$  (also written as  $S_1 \rightarrow \dots \rightarrow S_m \rightarrow \emptyset$ ) which will be referred as a *path*  $P$ . Let  $\bar{F}$  and  $R = -\log \bar{F}$  be the bundle component survival distribution and hazard function, respectively. The *signature* of this path and its *path coefficient* are defined as  $\nu(P) = m + 1$  and  $\sum_{k=1}^{\nu(P)-1} \left[ \sum_{i \in S_k \setminus S_{k+1}} R(x\lambda_i(S_k)) \right]$ , respectively, where  $x$  is the load per component in  $N$ .

Following [Lee, Durham and Lynch \(1995\)](#), the bundle survival distribution can written in terms of the path signatures and coefficients as

$$\bar{G}(x) = \sum_P (-1)^{\nu(P)} \exp \left\{ - \sum_{k=1}^{\nu(P)-1} \left[ \sum_{i \in S_k \setminus S_{k+1}} R(x\lambda_i(S_k)) \right] \right\}. \quad (7.1)$$

Since  $\bar{G}(0-) = 1$ , formula (7.1) shows that the survival distribution of the bundle strength is an affine mixture of over the path coefficients. If the component strength distribution is Weibull this affine mixture can be written as

$$\bar{G}(x) = \sum_P A_P \exp\{-C_P x^\rho\}, \quad (7.2)$$

where  $\rho$  is the Weibull shape parameter and  $A_P$  and  $C_P$  denote the affine and path coefficients, respectively, of the path  $P$  given above.

From (7.2) we will derive a gamma type of mixture for the density of the bundle strength distribution in the next subsection. To do this, replace  $x^\rho$  by  $y$

in (7.2). This gives

$$\bar{H}(y) = \sum_P A_P \exp\{-C_P y\} \equiv \int \exp(-\lambda y) dA(\lambda). \quad (7.3)$$

Note that this is the bundle strength distribution when the components strengths have an exponential distribution but the load-sharing rule is now  $(\lambda_i(M))^\rho$ .

**Remark: Daniels' Equal Load-Sharing Rule Daniels (1945)** Let  $X_1 < \dots < X_n$  denote the ordered component strengths. Then, under equal load-sharing, the bundle breaking strength is

$$\max_{j \leq n} \{(n-j+1)X_j/n\} = \sup_x x \bar{F}_n(x),$$

where  $F_n$  is the empirical cdf of the component strengths.

In addition, symmetry considerations lead to considerable simplification of formula (7.2) when the component survival distribution is Weibull with shape parameter  $\rho$ . This is our interest here for series circuits. In this case, we can just consider the number of working components,  $0, 1, \dots, n$ , rather than the set of working components. Since the contribution of  $k \rightarrow j$  where  $k > j$  is  $n^\rho (k-j)/k^\rho$  to the path coefficient, the path coefficient for path  $k_1 \rightarrow k_2 \rightarrow \dots \rightarrow k_t \rightarrow k_{t+1} = 0$  and its respective affine coefficient are

$$n^\rho \left[ \frac{(k_1 - k_2)}{k_1^\rho} + \dots + \frac{(k_{t-1} - k_t)}{k_{t-1}^\rho} + \frac{k_t}{k_t^\rho} \right] \text{ and } (-1)^{t+1} \binom{n}{k_1} \binom{k_1}{k_2} \dots \binom{k_{t-1}}{k_t} \binom{k_t}{k_t}.$$

## 7.2. The Bundle Strength Density as a Gamma Type of Mixed Distribution

The density  $h$  of  $H$  given by (7.3) is the affine mixture

$$\begin{aligned} h(y) &= \int \lambda \exp(-\lambda y) dA(\lambda) = \int \lambda \int_\lambda^\infty y \exp(-\theta y) d\theta dA(\lambda) \\ &= \int y \exp(-\theta y) \int_\theta^\infty \lambda dA(\lambda) d\theta \equiv \int y \exp(-\theta y) a_1(\theta) d\theta. \end{aligned}$$

Repeating the same interchange of order of integration  $n-2$  more times gives

$$h(y) = \int y^{n-1} \exp(-\theta y) a_{n-1}(\theta) d\theta \equiv \int \frac{\theta^n y^{n-1}}{(n-1)!} \exp(-\theta y) b(\theta) d\theta. \quad (7.4)$$

Formula (7.4) is a bona fide gamma mixture representation where the mixing is over the gamma scale parameter and where the mixing density,  $b(\theta)$ , is a sized biased convolution of uniforms (see [Durham and Lynch, 2000](#); [Li and Lynch, 2011](#), for details and interesting consequences of this representation).

Since  $G(y) = H(y^\rho)$ ,  $g(y) = \rho y^{\rho-1} h(y^\rho)$  is a gamma type mixture. Note that, from (7.4),

$$g(y) y^{-(n\rho-1)} = \rho \int \frac{\theta^n}{(n-1)!} \exp(-\theta y^\rho) b(\theta) d\theta \xrightarrow{y \rightarrow 0} \rho \int \frac{\theta^n}{(n-1)!} b(\theta) d\theta. \quad (7.5)$$

Formula (7.5) shows that the distribution of the breakdown strength of a series system of such bundles, a so-called *chain-of bundles*, is asymptotically Weibull with shape parameter  $n\rho$  and scale parameter based on the  $n$ th moment of  $b(\theta)$ .

### 7.3. The Gibbs Representation of the Distribution of the States of a Bundle

Below is a summary of results from Sections 2 and 4 in [Li, Gleaton and Lynch \(2019\)](#) (see also [Li and Lynch \(2019\)](#)). Here, the set,  $A$ , denotes the set of working components in the bundle that work under a load per component  $s$  and  $A^c$ , the complement of  $A$ , is the set that has failed.

A starting point is to model the probability that the set of working components,  $P_s(A)$ , as a *Gibbs measure with energy*  $U_s(A)$ ,  $A \subseteq N$  with  $U_s(\emptyset) = 0$ , where

$$P_s(A) = \frac{\exp\{-U_s(A)\}}{Z(s)}. \quad (7.6)$$

Here, the normalizing constant  $Z(s) = \sum_{A \subseteq N} \exp\{-U_s(A)\} = 1/P_s(\emptyset)$  is referred to as the *partition function* in statistical mechanics and is just the reciprocal of the probability that none of the components work under a load per component  $s$ .

The *local structure* of  $P_s(A)$  defined in (7.6) is the log odds for component  $i \in A$ . An attractive feature of load-sharing systems is that the local structure is simply

$$\sigma_i(A, s) \equiv \log \frac{P_s(A)}{P_s(A - \{i\})} = \log \frac{\bar{F}_i(\lambda_i(A)s)}{\bar{F}_i(\lambda_i(A)s)}. \quad (7.7)$$

If  $U_s(A)$  is the energy, define its *potential*  $V_s(A)$  as

$$V_s(A) \equiv - \sum_{B \subseteq A} (-1)^{|A-B|} U_s(B), \quad (7.8)$$

where  $|A|$  denotes the cardinality of the set  $A$ . We have immediately

$$U_s(A) \equiv - \sum_{B \subseteq A} V_s(B) \quad (7.9)$$

since (7.8) and (7.9) are just the Möbius inversion formulas that relate  $U_s$  and  $V_s$ .

Thus, from (7.6), (7.7) and (7.9),

$$\begin{aligned} \sigma_i(A, s) &= \log \frac{P_s(A)}{P_s(A - \{i\})} = U_s(A - \{i\}) - U_s(A) \\ &= \sum_{L \subseteq A} V_s(L) - \sum_{L \subseteq A - \{i\}} V_s(L) \\ &= \sum_{L \subseteq A: i \in L} V_s(L). \end{aligned} \quad (7.10)$$

Identity (7.10) gives a way to calculate the log odds ratios by summing potentials. The following theorem shows, via the Möbius inversion formula, how to obtain the potentials from the log odds ratios.

**Theorem 4.1** (Li, Gleaton and Lynch, 2019, Theorem 2.1) Let  $\sigma_s(A) \equiv \sum_{i \in A} \sigma_i(A, s)$ . Then, for  $L \neq \emptyset$ ,

$$V_s(L) = \frac{\sum_{A \subseteq L} (-1)^{|L \setminus A|} \sigma_s(A)}{|L|}. \quad (7.11)$$

There is some simplification in the quantities  $U(A)$ ,  $V(A)$  and  $\sigma(A)$  defined above when the load-sharing rule is the equal load-sharing rule; they only depend on  $|A|$ . This is useful in the situation we consider here where the details are spelled out in the following example.

**Example:** (i) Consider series circuits of capacitors of equal capacitance under increasing voltage load. Thus, the equal load-sharing rule,  $\lambda_i(A) = n/|A|$ , applies. Furthermore, it is assumed that the capacitors have BD voltages whose survival function is  $\bar{W}(x; \tau, \rho) = \exp\{-(x/\tau)^\rho\} \equiv \bar{W}(x)$ .

Then, if  $|A| = a$ , (7.7) becomes

$$\sigma_i(A, s) = \log \frac{\bar{F}(ns/|A|)}{\bar{F}(ns/|A|)} \equiv \sigma^*(|A|, s) \text{ for } i \in A, \quad (7.12)$$

and also, if  $|L| = l$ , then (7.11) becomes

$$V_s(L) = \frac{\sum_{a \leq l} (-1)^{l-a} a \sigma^*(a, s)}{l} \equiv V_s^*(l), \quad (7.13)$$

where  $a \sigma^*(a, s) = \sigma_s(A)$  in Theorem 4.1 for  $i \in A \subseteq L$ .

Thus, from (7.9), (7.12), (7.13),

$$U_s(A) \equiv - \sum_{B \subseteq A} V_s(B) = - \sum_{B \subseteq A} V_s^*(|B|) = - \sum_{B \leq |A|} \binom{a}{b} V_s^*(b) \equiv U_s^*(a). \quad (7.14)$$

From (7.6), (7.12), (7.13) and (7.14), if  $|A| = a$ , then

$$P_s(A) = \frac{\exp\{-U_s^*(a)\}}{Z(s)} \text{ and } p_{a,s} = P_s(\{A : \forall |A| = a\}) = \binom{n}{a} \frac{\exp\{-U_s^*(a)\}}{Z(s)} \quad (7.15)$$

where  $p_{a,s}$  is the probability distribution of the number of working capacitors.

(ii) Furthermore, when the capacitors have BD voltages whose survival function is

$\bar{W}(x; \tau, \rho) = \exp\{-(x/\eta)^\rho\} \equiv \bar{W}(x)$ . Then, (7.12) becomes

$$\begin{aligned}
 \sigma_i(A, s) &= \log \frac{\bar{W}(\lambda_i(A)s)}{\bar{W}(\lambda_i(A)s)} = -\left(\frac{|A|}{\tau}\right)^\rho s^\rho - \log \left(1 - \exp\left\{-\left(\frac{|A|}{\tau}\right)^\rho s^\rho\right\}\right) \\
 &= \sigma^*(|A|, s) \text{ for } i \in A \\
 &= -\left(\frac{|A|}{\tau}\right)^\rho s^\rho - \log \left(\left(\frac{|A|}{\tau}\right)^\rho s^\rho (1 + o(1))\right) \\
 &= -\left(\frac{|A|}{\tau}\right)^\rho s^\rho - \log \left(\frac{|A|}{\tau}\right)^\rho - \rho \log s + o(1).
 \end{aligned}$$

**Remark: Description of the stochastic failure process for the bundle**

The failure of components is a failure of two types of component failures as the load increases. As the load increases, a component fails due to the increasing load. We refer to this as a Phase I failure. When this component fails it can cause a sequence of components failures (Phase II failures) due to load transfer from the Phase I failure and the sequence of failures in the Phase II cycle. The bundle fails through a sequence of Phase I/II cycles.

Let  $N^*$  denote the collection of working components right after a Phase I failure. Then, the Gibbs measure for the sub-bundle  $N^*$  gives the distribution for the set of components that survive after the Phase II cycle for the Phase I failure. If the load per component is  $s$  when the Phase I failure occurs, then the load per component on the sub-bundle is  $Ns/N^*$ .

## 8. Statistical Analysis of [Kim and Lee \(2004\)](#)'s Data

In this section, we consider the data<sup>3</sup> from Figures 3, 6 and 14 in [Kim and Lee \(2004\)](#) as well as their Weibull analyses of these figures and [Le \(2012\)](#)'s analysis of their Figure 14 (Figures 4 and 5 of [Le \(2012\)](#)). We use this data to see the role that the Weibull plays in their analysis, the physical interpretation of the Weibull shape and scale, and the BD formalism. In addition, other distributions are used to compare with the Weibull and to study the legitimacy of some of the BD formalism assumptions.

### 8.1. Fitting Breakdown Data with Different Statistical Distributions

In this section, we consider the lifetime data of  $\text{HfO}_2$  based gate dielectrics (gate area  $\approx 4 \times 10^{-4} \text{ mm}^2$  and thickness  $\approx 4.8 - 5 \text{ nm}$ ) presented in [Kim and Lee \(2004\)](#)'s Figure 14 (see also [Le, 2012](#), Figure 4) with different frequency unipolar AC voltage stresses (10 kHz and 0.1 kHz) and different duty cycles  $T_{\text{on}}/T_0 = 0.1$  and 0.5, where  $T_0$  is the duration of each cycle and  $T_{\text{on}}$  is the duration of the 'on' period in each cycle.

---

<sup>3</sup>The data used here for Figures 3 and 6 are constructed from the figures. We want to thank Professor Jack C. Lee for his efforts, though unsuccessful, in trying to provide this data. We also want to thank Professor Jia-Liang Le for the cycles to failure data for Figure 14 that he used in his Figure 4 Weibull plots.

Different lifetime distributions are fitted to the data. The following lifetime distributions are considered:

- Weibull distribution with cumulative distribution function (CDF):

$$F_W(t; \eta, \beta) = 1 - \exp \left[ - \left( \frac{t}{\eta} \right)^\beta \right], \quad t > 0.$$

- Lognormal distribution with CDF:

$$F_{LN}(t; \mu_N, \sigma_N) = \Phi \left( \frac{\ln t - \mu_N}{\sigma_N} \right), \quad t > 0,$$

where  $\Phi(z)$  is the CDF of the standard normal distribution.

- Loglogistic distribution with CDF:

$$F_{LL}(t; \mu_L, \sigma_L) = \frac{\exp \left( \frac{\ln t - \mu_L}{\sigma_L} \right)}{1 + \exp \left( \frac{\ln t - \mu_L}{\sigma_L} \right)}, \quad t > 0.$$

- Birnbaum-Saunders distribution with CDF:

$$F_{BS}(t; \alpha, \gamma) = \Phi \left\{ \frac{1}{\alpha} \left[ \left( \frac{t}{\gamma} \right)^{1/2} - \left( \frac{\gamma}{t} \right)^{1/2} \right] \right\}, \quad t > 0.$$

TABLE 1  
Parameter estimates of different distributions for the data in (Kim and Lee, 2004, Figure 14)

Distribution		10kHz	10kHz	0.1kHz
	$T_{on}/T_0 = 0.1$	$T_{on}/T_0 = 0.5$	$T_{on}/T_0 = 0.1$	
Weibull	$\hat{\eta}$	81.989	222.645	263.030
	$\hat{\beta}$	2.799	2.575	3.098
	MTTF	73.006	197.700	235.221
	$-2 \ln L$	189.044	<b>232.610</b>	232.513
Lognormal	$\hat{\mu}_N$	4.213	5.180	5.395
	$\hat{\sigma}_N$	0.399	0.483	0.364
	MTTF	73.137	199.683	235.471
	$-2 \ln L$	188.513	234.880	232.158
Loglogistic	$\hat{\mu}_L$	4.216	5.220	5.409
	$\hat{\sigma}_L$	0.223	0.277	0.210
	MTTF	73.636	210.592	240.443
	$-2 \ln L$	<b>188.459</b>	235.434	232.931
Birnbaum-Saunders	$\hat{\alpha}$	0.408	0.496	0.369
	$\hat{\gamma}$	67.261	175.506	219.847
	MTTF	72.851	197.074	234.804
	$-2 \ln L$	188.598	234.746	<b>232.038</b>

In Table 1, we tabulate the parameter estimates for the different fitted distributions as well as their mean time to failure (MTTF) estimates and log-likelihoods ( $-2 \ln L$ ). The values of the MTTF estimates and the  $-2 \ln L$ 's are

Kim and Lee's Figure 14: Probability Plot in Weibull Scale

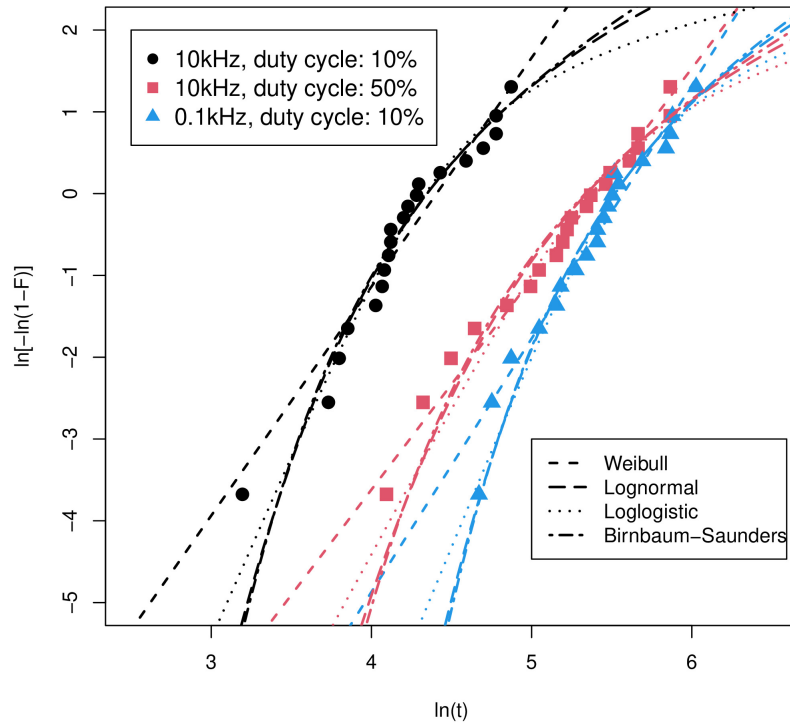


FIG 1. Probability plot of different fitted parametric models for the data from [Kim and Lee \(2004\)](#)'s Figure 14 in Weibull scale

all comparable. The values of the Weibull shapes are comparable to those in [Kim and Lee \(2004\)](#)'s Figure 14 where the range is given as 2.4 to 2.9. The fitted distributions presented in Table 1 are plotted in the probability plot in Weibull scale in Figure 1.

As noted in Sections 4 and 6, the Weibull shape parameter is related to the thickness of the capacitor. Here, we are considering static cycle testing. Thus, the shape is proportional to the thickness while the scale/characteristic lifetime depends on the cyclic protocol. For pure crystalline  $\text{HfO}_2$  the proportionality constant is the crystalline lattice constant (see Section 3) which is about 1. Since the thickness is about 4.9 nm, if the dielectric is pure crystalline the shape parameter would be around 5. As noted in Section 3, in modern  $\text{HfO}_2$  dielectrics BD begins in the grain boundaries, not in the (pure crystalline) grains. This would reduce the shape parameter and is consistent with [Kim and Lee \(2004\)](#)'s discussion of their Figure 10 regarding this. [Le \(2012\)](#)'s analysis suggested it is a “size effect” and is reflected in the “curvature” in [Le \(2012\)](#)'s Figure 4.

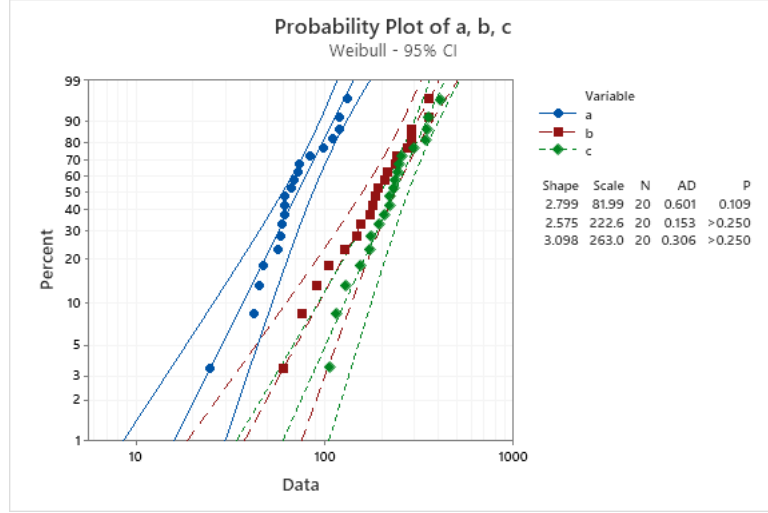


FIG 2. Weibull probability plot of the data from [Kim and Lee \(2004\)](#)'s Figure 14 in Weibull scale (a) 10kHz,  $T_{on}/T_0 = 0.1$  (b) 10kHz,  $T_{on}/T_0 = 0.5$  (c) 0.1kHz,  $T_{on}/T_0 = 0.1$

The curvature is not confirmed in the Weibull plots with 95% confidence bands in Figure 2 where the  $p$ -values for the Anderson-Darling (AD) indicate the Weibull's goodness-of-fit. We discuss “size effect” issues in Section 10.

### 8.2. Breakdown-Time Regression Models

Below we consider Weibull and semiparametric proportional hazards models to investigate the validity of the Weakest Link Principles A.1 and A.1'. The analyses, below, do not refute the A.1' Weakest Link Principle of the BD formalism for both EOTs but the Weibull analysis does refute the A.1 Weakest Link Principle for  $EOT = 1.4$  nm and suggests that the principle depends on the thickness of the dielectric. The analyses cannot be any more definitive since all but one of the confidence intervals are so large because of the small sample sizes.

#### 8.2.1. Proportional hazards models for [Kim and Lee \(2004\)](#)'s Figure 6 data

For the data in Figure 6 of [Kim and Lee \(2004\)](#), there are two covariates, area and the equivalent oxide thickness (EOT), that are considered to be related to

the breakdown voltage ( $V_{BD}$ ):

$$\begin{aligned} \text{Area: } x_1 &= \begin{cases} 1.6 \times 10^{-5} \text{ cm}^2, \\ 0.1 \times 10^{-5} \text{ cm}^2; \end{cases} \\ \text{EOT: } x_2 &= \begin{cases} 1.4 \text{ nm}, \\ 2.5 \text{ nm}. \end{cases} \end{aligned}$$

#### Parametric Proportional Hazards Model

First, we consider a parametric proportional hazards model (i.e., Weibull regression model) for the breakdown voltage data presented in Figure 6 of [Kim and Lee \(2004\)](#) as follows:

$$\begin{aligned} \Pr(V_{BD} < v) &= F_W(v; \rho(x_2), \tau(\mathbf{x})) \\ &= 1 - \exp \left[ - \left( \frac{v}{\tau(\mathbf{x})} \right)^{\rho(x_2)} \right], \quad v > 0, \end{aligned} \quad (8.1)$$

where  $\rho(x_2)$  is the shape parameter depending on the EOT and  $\tau(\mathbf{x})$  is the scale parameter depending on both the area and the EOT. We use the link functions

$$\begin{aligned} \tau(\mathbf{x}) &= \exp(\nu_0 + \nu_1 x_1 + \nu_2 x_2), \\ \rho(x_2) &= \frac{1}{\gamma_0 + \gamma_1 x_2}. \end{aligned}$$

Based on the breakdown voltage data presented in Figure 6 of [Kim and Lee \(2004\)](#), we obtain the maximum likelihood estimates of the model parameters as

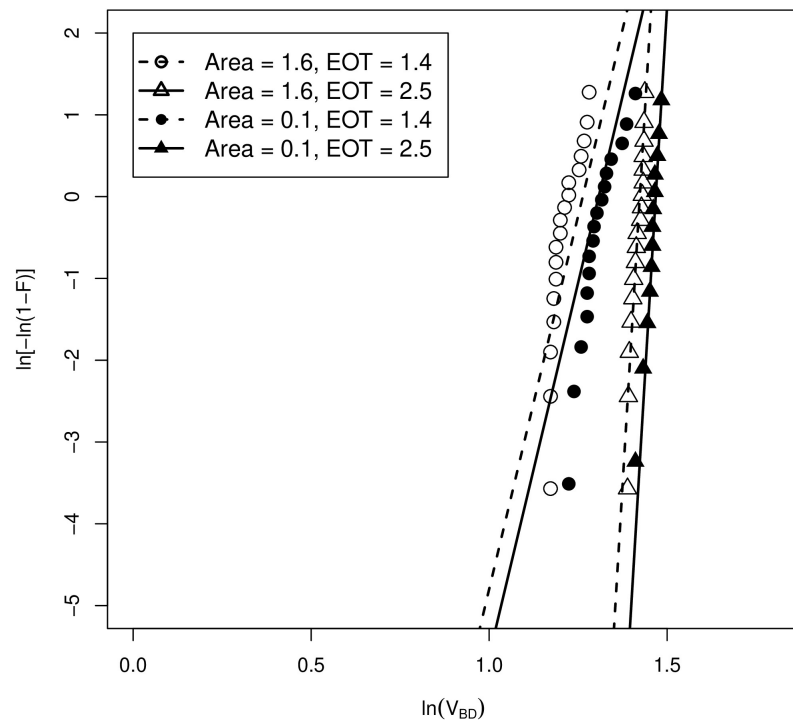
$$\begin{aligned} \hat{\nu}_0 &= 1.10671, \hat{\nu}_1 = -0.02979, \hat{\nu}_2 = 0.14570, \\ \hat{\gamma}_0 &= 0.10702, \hat{\gamma}_1 = -0.03731. \end{aligned}$$

The  $p$ -values of testing each of the parameters  $\gamma_0, \gamma_1, \nu_0, \nu_1, \nu_2$  are different from 0 are all  $< 10^{-8}$ , which indicate that the parameters are statistically significant.

The Weibull probability plot of the breakdown voltage data presented in Figure 6 of [Kim and Lee \(2004\)](#) with the fitted models are presented in Figure 3. In summary, the MLEs of Weibull parameters for different areas and EOTs are as follows:

- Area =  $1.6 \times 10^{-5} \text{ cm}^2$ , EOT = 1.4 nm: Shape parameter  $\hat{\rho} = 18.2536$ ; Scale parameter  $\hat{\tau} = 3.5361$ ;
- Area =  $1.6 \times 10^{-5} \text{ cm}^2$ , EOT = 2.5 nm: Shape parameter  $\hat{\rho} = 72.7921$ ; Scale parameter  $\hat{\tau} = 4.1507$ ;
- Area =  $0.1 \times 10^{-5} \text{ cm}^2$ , EOT = 1.4 nm: Shape parameter  $\hat{\rho} = 18.2536$ ; Scale parameter  $\hat{\tau} = 3.6977$ ;
- Area =  $0.1 \times 10^{-5} \text{ cm}^2$ , EOT = 2.5 nm: Shape parameter  $\hat{\rho} = 72.7921$ ; Scale parameter  $\hat{\tau} = 4.3404$ .

Kim and Lee Figure 6 – Fitted by Weibull Regression Model

FIG 3. Weibull probability plot of the data from [Kim and Lee \(2004\)](#)'s Figure 6

To evaluate the effect of the area, based on the proportional hazards assumption in the Weibull regression model, we have

$$\Pr(T > t; x_1 = 1.6, x_2) = \Pr(T > t; x_1 = 0.1, x_2)]^{\phi(x_2)},$$

where  $\phi(x_2)$  is the proportionality constant for a fixed EOT (i.e.,  $x_2$ ). The proportionality constant, if it is an integer (say,  $n$ ), can be interpreted as the number of independent and identically distributed components in a series system in which

$$\Pr(n\text{-component series system lifetime} > t) = [\Pr(\text{component lifetime} > t)]^n.$$

For  $EOT = 1.4 \text{ nm}$  and  $2.5 \text{ nm}$ , we have  $\phi(1.4) = 2.2606$  and  $\phi(2.5) = 25.8563$ , with 95% normal approximated confidence intervals  $(1.2650, 3.2562)$  and  $(0, 214.4775)$ , respectively. Since 16 is not in the 95% confidence interval  $(1.2650, 3.2562)$ , the A.1 Weakest Link Principle for this thickness is rejected for  $EOT = 1.4 \text{ nm}$ .

#### Semiparametric Proportional Hazards Model

In addition to fitting [Kim and Lee \(2004\)](#)'s Figure 6 data by using a parametric proportional hazards model, we consider the Cox semiparametric proportional hazard model here.

In analogy to the parametric proportional hazard model in Eq. (8.1) that the proportionality constant for area effect depends on the EOT, we consider the semiparametric Cox proportional hazards model with an interaction term, i.e.,

$$h(t; x_1, x_2) = h(t; x_{10}, x_{20}) \exp(\theta_1 x_1 + \theta_2 x_2 + \theta_{12} x_1 x_2), \quad t > 0, \quad (8.2)$$

where  $h(t; x_1, x_2)$  is the hazard function at time  $t$  with covariates  $(x_1, x_2)$ ,  $(x_{10}, x_{20})$  are the baseline covariates and  $\boldsymbol{\theta} = (\theta_1, \theta_2, \theta_{12})$  is the vector of parameters. Alternatively, we can express the Cox proportional hazards model in Eq. (8.2) in terms of the survival probabilities as

$$\Pr(T > t; x_1, x_2) = \Pr(T > t; x_{10}, x_{20})]^{\exp(\theta_1 x_1 + \theta_2 x_2 + \theta_{12} x_1 x_2)}. \quad (8.3)$$

Based on [Kim and Lee \(2004\)](#)'s Figure 6 data, we obtain the estimates of  $\boldsymbol{\theta}$  as  $\hat{\boldsymbol{\theta}} = (\hat{\theta}_1, \hat{\theta}_2, \hat{\theta}_{12}) = (1.0500, -4.9421, 0.3469)$ . For  $EOT = 1.4 \text{ nm}$  and  $2.5 \text{ nm}$ , we have the proportionality constants for the area as

$$\begin{aligned} \exp[(1.6 - 0.1)\hat{\theta}_1 + 1.4(1.6 - 0.1)\hat{\theta}_{12}] &= 10.0107 \\ \text{and } \exp[(1.6 - 0.1)\hat{\theta}_1 + 2.5(1.6 - 0.1)\hat{\theta}_{12}] &= 17.7454, \end{aligned}$$

with 95% normal approximated confidence intervals  $(0, 37.1487)$  and  $(0, 83.5950)$ , respectively. The fitted survival curves based on Cox proportional hazards model are presented in Figure 4.

#### 8.2.2. Fitting [Kim and Lee \(2004\)](#)'s Figure 3 data with different parametric models and link functions

In Figure 3 of [Kim and Lee \(2004\)](#), the soft breakdown (SBD) and hard breakdown (HBD) of  $\text{HfO}_2$  ( $EOT = 1.4 \text{ nm}$ ) at different stress voltages (-2.6V, -2.7V

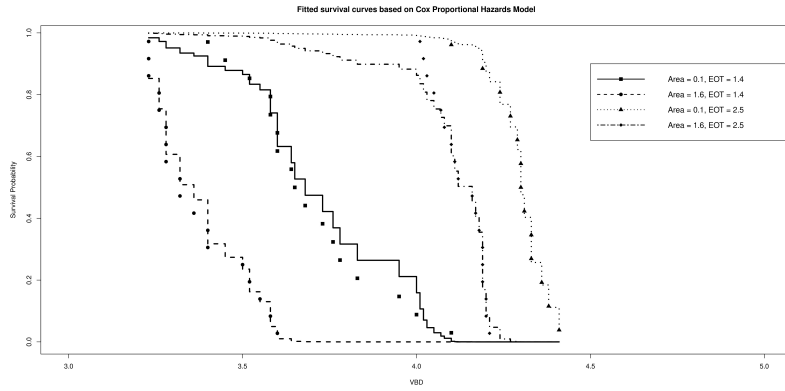


FIG 4. Fitted survival curves based on Cox proportional hazards model

and  $-2.8V$ ) are presented. To fit the data with a lifetime regression model, we define the following variables

$$\begin{aligned} z_1 &= \begin{cases} 0 & \text{for SBD,} \\ 1 & \text{for HBD,} \end{cases} \\ z_2 &= -\text{voltage stress.} \end{aligned}$$

#### Weibull Regression Model

We assume that the SBD and HBD follow Weibull distributions with different shape and scale parameters. A Weibull regression model with covariates  $z_1$  and  $z_2$  can be expressed as

$$\begin{aligned} \Pr(T < t; \rho(\mathbf{z}), \tau(\mathbf{z})) &= F_W(t; \rho(\mathbf{z}), \tau(\mathbf{z})) \\ &= 1 - \exp \left[ - \left( \frac{v}{\tau(\mathbf{z})} \right)^{\rho(\mathbf{z})} \right], \quad t > 0, \end{aligned} \quad (8.4)$$

where  $\rho(\mathbf{z})$  is the shape parameter and  $\tau(\mathbf{z})$  is the scale parameter. For the scale parameter, based on the power law relationship, we consider a log-linear link function

$$\tau(\mathbf{z}) = \exp(\nu_0 + \nu_1 z_1 + \nu_2 \ln z_2). \quad (8.5)$$

For the shape parameter, in order to study the effect of different relations between the covariates and the shape parameter, we consider the following link functions:

- Log-linear:  $\rho_{LL}(\mathbf{z}) = \exp(\delta_0 + \delta_1 z_1 + \delta_2 \ln z_2);$
- Linear:  $\rho_L(\mathbf{z}) = \delta_0 + \delta_1 z_1 + \delta_2 \ln z_2;$
- Inverse linear:  $\rho_{IL}(\mathbf{z}) = (\delta_0 + \delta_1 z_1 + \delta_2 \ln z_2)^{-1}.$

We also consider the Weibull regression models in which the Weibull shape parameter does not depend on the voltage stress (i.e.,  $\delta_2 = 0$ ). The maximum likelihood estimates and the  $p$ -values for testing the significance of parameters for Weibull regression model with different link functions are presented in Table 2. The values of the likelihood for different models are also presented in Table 2.

We observe that the results with different link functions are similar, especially in the estimates of MTTF. Moreover, the shape parameters for SBD and HBD are around 1.4 and 2.0, which agree with the results obtained in [Kim and Lee \(2004\)](#).

TABLE 2  
Maximum likelihood estimates and the  $p$ -values for testing the significance of parameters for Weibull regression model with different link functions

Est.	With voltage as a covariate for the shape parameter				Without voltage as a covariate for the shape parameter (i.e., $\delta_2 = 0$ )			
	$\rho_{LL}(\mathbf{z})$	$p$ -value	$\rho_L(\mathbf{z})$	$p$ -value	$\rho_{LL}(\mathbf{z})$	$p$ -value	$\rho_L(\mathbf{z})$	$p$ -value
$\delta_0$	0.9926	0.3220	2.3585	0.2280	0.3907	0.3539	0.3538	0.0001
$\delta_1$	0.3208	0.0107	0.5388	0.0132	-0.1928	0.0113	0.3218	0.0105
$\delta_2$	-0.6413	0.3831	-0.9373	0.3839	0.3126	0.3828	0.3828	0.0129
$\nu_0$	53.1708	0.0000	54.0436	0.0000	54.0537	0.0000	53.9475	0.0000
$\nu_1$	1.9314	0.0000	-1.9315	0.0000	1.9321	0.0000	1.9323	0.0000
$\nu_2$	-50.0240	0.0000	-49.9933	0.0000	-49.9063	0.0000	-49.7994	0.0000
SBD, -2.6V								
$\hat{\rho}$	1.4620		1.4628		1.4505		1.4245	
$\hat{\tau}$	585.4282		584.7454		582.6511		580.2213	
MTTF	530.2220		529.5652		528.2759		527.4334	
HBD, -2.6V								
$\hat{\rho}$	2.0150		2.0016		2.0136		1.9651	
$\hat{\tau}$	4039.0270		4034.5050		4022.4910		4006.7440	
MTTF	3579.0320		3575.4350		3564.4180		3552.1640	
SBD, -2.7V								
$\hat{\rho}$	1.4271		1.4275		1.4261		1.4245	
$\hat{\tau}$	88.6257		88.6249		88.5978		88.5846	
MTTF	80.5410		80.5372		80.5238		80.5253	
HBD, -2.7V								
$\hat{\rho}$	1.9668		1.9662		1.9669		1.9651	
$\hat{\tau}$	611.4525		611.4758		611.6590		611.7249	
MTTF	542.0706		542.0948		542.2529		542.3224	
SBD, -2.8V								
$\hat{\rho}$	1.3942		1.3934		1.4033		1.4245	
$\hat{\tau}$	14.3704		14.3863		14.4274		14.4814	
MTTF	13.1061		13.1218		13.1446		13.1639	
HBD, -2.8V								
$\hat{\rho}$	1.9215		1.9321		1.9239		1.9651	
$\hat{\tau}$	99.1449		99.2504		99.6037		100.0020	
MTTF	87.9475		88.0354		88.3512		88.6564	
LL	-117.8087		-117.8129		-117.8089		-117.8400	
SBD, -2.8V								
$\hat{\rho}$	1.9215		1.9321		1.9239		1.9651	
$\hat{\tau}$	99.1449		99.2504		99.6037		100.0020	
MTTF	87.9475		88.0354		88.3512		88.6564	
LL	-117.8087		-117.8129		-117.8089		-117.8400	

### Lognormal Regression Model

We assume that the SBD and HBD follow lognormal distributions with different shape and scale parameters. A lognormal regression model with covariates  $z_1$  and  $z_2$  can be expressed as

$$\begin{aligned} \Pr(T < t; \mu(\mathbf{z}), \sigma(\mathbf{z})) &= F_{LN}(t; \mu(\mathbf{z}), \sigma(\mathbf{z})) \\ &= \Phi \left[ \frac{\ln t - \mu(\mathbf{z})}{\sigma(\mathbf{z})} \right], \quad t > 0, \end{aligned} \quad (8.6)$$

where  $\Phi(\cdot)$  is the cumulative distribution function of the standard normal distribution,  $\sigma(\mathbf{z})$  is the shape parameter and  $\mu(\mathbf{z})$  is the scale parameter. For the scale parameter, based on the power law relationship, we consider a log-linear link function

$$\mu(\mathbf{z}) = \exp(\nu_0 + \nu_1 z_1 + \nu_2 \ln z_2). \quad (8.7)$$

For the shape parameter, in order to study the effect of different relations between the covariates and the shape parameter, we consider the following link functions:

- Log-linear:  $\sigma_{LL}(\mathbf{z}) = \exp(\delta_0 + \delta_1 z_1 + \delta_2 \ln z_2)$ ;
- Linear:  $\sigma_L(\mathbf{z}) = \delta_0 + \delta_1 z_1 + \delta_2 \ln z_2$ ;
- Inverse linear:  $\sigma_{IL}(\mathbf{z}) = (\delta_0 + \delta_1 z_1 + \delta_2 \ln z_2)^{-1}$ .

We also consider the lognormal regression models in which the shape parameter does not depend on the voltage stress (i.e.,  $\delta_2 = 0$ ). The maximum likelihood estimates and the  $p$ -values for testing the significance of parameters for lognormal regression model with different link functions are presented in Table 3. The values of the likelihood for different models are also presented in Table 3.

TABLE 3  
Maximum likelihood estimates and the  $p$ -values for testing the significance of parameters for lognormal regression model with different link functions

Est.	With voltage as a covariate for the shape parameter				Without voltage as a covariate for the shape parameter (i.e. $\delta_2 = 0$ )			
	$\sigma_{LL}(\mathbf{z})$	p-value	$\sigma_L(\mathbf{z})$	p-value	$\sigma_{LL}(\mathbf{z})$	p-value	$\sigma_L(\mathbf{z})$	p-value
$\delta_0$	0.6460	0.3909	2.0565	0.0857	-1.4026	0.3381	-0.2648	0.0023
$\delta_1$	-0.2573	0.0245	-0.1770	0.0248	0.3986	0.0236	-0.2679	0.0215
$\delta_2$	-0.9376	0.3450	-1.3009	0.1947	2.7325	0.2103	-0.1806	0.0230
$\nu_0$	5.8624	0.0000	52.9790	0.0000	53.0099	0.0000	53.4532	0.0000
$\nu_1$	2.0240	0.0000	2.3251	0.0000	2.3554	0.0000	2.0233	0.0000
$\nu_2$	-50.0891	0.0000	-49.2045	0.0000	-49.2366	0.0000	-49.6522	0.0000
SBD, -2.6V								
$\hat{\sigma}$	0.7788		0.8134		0.8276		0.7673	
$\hat{\mu}$	6.0013		5.9635		5.9637		5.9867	
MTTF	547.0701		541.5037		547.9512		534.3846	
HBD, -2.6V								
$\hat{\sigma}$	0.6021		0.6364		0.6223		0.5870	
$\hat{\mu}$	8.0223		7.9886		7.9891		8.0100	
MTTF	3653.9350		3608.9280		3578.7860		3577.0890	
SBD, -2.7V								
$\hat{\sigma}$	0.7518		0.7514		0.7625		0.7673	
$\hat{\mu}$	4.1109		4.1065		4.1055		4.1079	
MTTF	80.9211		81.3391		81.1452		81.6430	
SBD, -2.7V								
$\hat{\sigma}$	0.5812		0.5873		0.5848		0.5870	
$\hat{\mu}$	6.1319		6.1317		6.1309		6.1313	
MTTF	545.0053		546.8269		545.6207		546.5059	
SBD, -2.8V								
$\hat{\sigma}$	0.7266		0.7170		0.7088		0.7673	
$\hat{\mu}$	2.2893		2.3171		2.3149		2.2975	
MTTF	12.8485		13.1200		13.0151		13.3555	
HBD, -2.8V								
$\hat{\sigma}$	0.5617		0.5400		0.5527		0.5870	
$\hat{\mu}$	4.3103		4.3422		4.3403		4.3208	
MTTF	87.1856		88.9446		89.3928		89.3999	
LL	-116.1585		-116.0007		-116.0017		-116.3284	
							-116.3264	
							-116.3264	

### 8.3. Prediction of Hard Breakdown based on Soft Breakdown Time

Based on the SBD and HBD data in Figure 3 of [Kim and Lee \(2004\)](#), we are interested in predicting the HBD based on SBD. As [Kim and Lee \(2004\)](#) suggested, “the time between soft and hard breakdown significantly decreases as stress voltage increases”; therefore, to predict HBD based on the observed SBD, we should take the stress voltage into account.

Due to the strong linear relation between the log-transformed HBD and log-transformed SBD, we consider a simple linear regression of  $\ln(HBD)$  on  $\ln(SBD)$  and the voltage stress (i.e.,  $z_2$ ):

$$\ln(HBD) = \beta_0 + \beta_1 \ln(SBD) + \beta_2 z_2, \quad (8.8)$$

where  $\beta_0$ ,  $\beta_1$  and  $\beta_2$  are the regression parameters. Based on the data in Figure 3 of [Kim and Lee \(2004\)](#), we obtain the estimates of the regression parameters as  $\hat{\beta}_0 = 15.1795$ ,  $\hat{\beta}_1 = 0.7487$  and  $\hat{\beta}_2 = -4.4881$  with the corresponding  $p$ -values for testing the significant as  $4.61e - 16$ ,  $< 2e - 16$  and  $1.70e - 13$ , respectively. The original data and the fitted regression lines are presented in Figure 5.

In addition, Figure 6 indicates the linear relationship between log percentile and  $\ln V$  given in Consequences of A.2 & A.3 (ii) of the BD formalism.

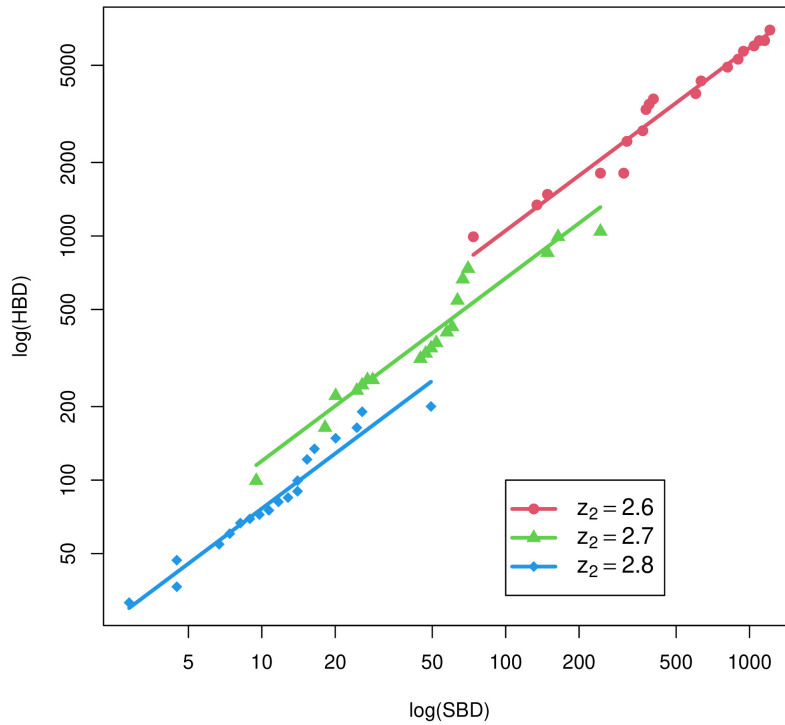
**Simple linear regression for predicting HBD based on SBD**

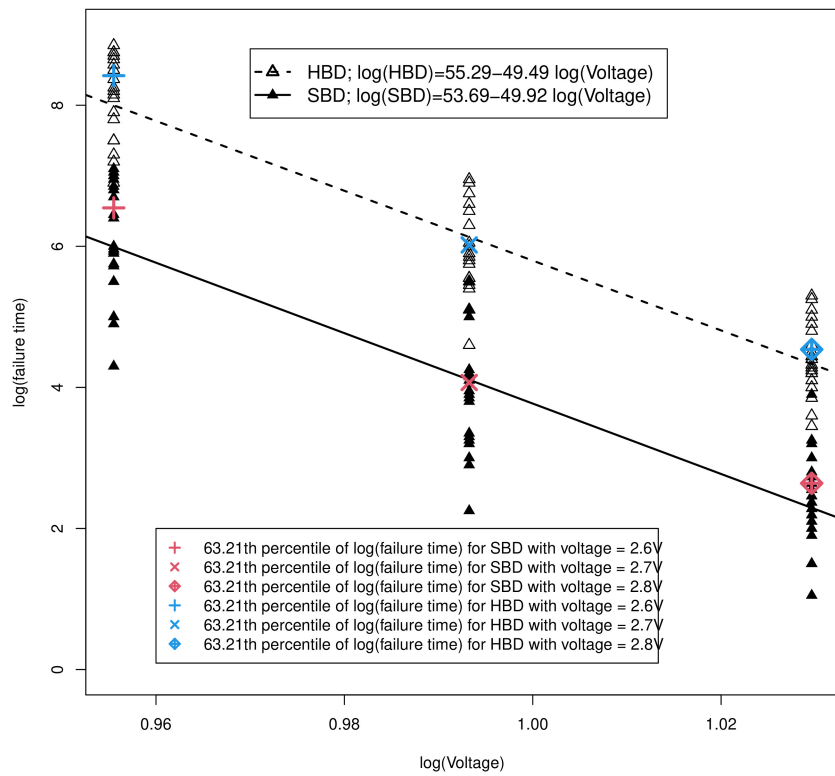
FIG 5. Simple linear regression of [Kim and Lee \(2004\)](#)'s Figure 3 data for predicting HBD based on SBD and voltage stress

## 9. Circuits of Ordinary Capacitors

In this section, we illustrate how the BD distributional behavior of ordinary capacitors affects that of a series circuit of such capacitors. In Section 9.1, we investigate the VBD of the circuit where the VBD distribution is Weibull. The parameters are based on the earlier analysis of [Kim and Lee \(2004\)](#)'s Figure 6 data for illustrative purposes even though the data is not for ordinary capacitors but for thin-dielectrics.

We also examine simulation size effects and chain-of-bundles (parallel-series circuits) size effects for these capacitors in Sections 6.2 and 6.4. Such effects are related to finite weakest link models considered by [Le, Bažant and Bazant \(2009\)](#), [Le \(2012\)](#) and [Bažant and Le \(2017\)](#) for dielectrics and related models for finite length chains considered earlier by [Phoenix \(1983\)](#), [Phoenix and Tierney \(1983\)](#) and [Taylor \(1987\)](#) for polymer fibers. This was discussed in Section 4.

Since the testing protocol for [Kim and Lee \(2004\)](#)'s Figure 6 is increasing

FIG 6. Relationship between log-failure-time and  $\log(V)$

voltage load, VBD, the analysis is greatly simplified (e.g., Daniels formula in Section 7 applies) than that for circuits based on [Kim and Lee \(2004\)](#)'s Figures 3 and 14 data. In these latter two data sets, the respective protocols are the time to BD (TBD) and cycle times to BD (CTBD) under static voltage loads. Recall that the AC amplitude is constant over the "on" period in a duty cycle for the static case of cycles to failure.

In Section 9.3, we discuss how the distributional behavior of ordinary capacitors can be used to access the TBD or CTBD reliability of that of a series circuit for static loads on the circuit. In Section 10, we discuss size effects related to [Kim and Lee \(2004\)](#)'s Figure 14 ([Le \(2012\)](#)'s Figure 4).

### 9.1. VBD of Series and Parallel Circuits Based on [Kim and Lee \(2004\)](#)'s Figure 6 Data

Here, we illustrate the statistical behavior of the BD of series and parallel circuits for ordinary capacitors whose breakdown distributions are based on the Weibull fits for Kim and Lee's Figure 6 data. In Figures 7 and 8, exact Weibull plots and survival distributions are given for series circuits of two of these capacitors.

The curvature in the Weibull plots is due to the fact that the distribution has a mixed gamma-type of distribution with density of the form (7.5). Note that the plots for the series circuits suggest that mixtures of two truncated Weibulls will be a very good empirical approximation similar to the grafted distribution suggested by [Le \(2012\)](#) and [Bažant and Le \(2017\)](#) for [Kim and Lee \(2004\)](#)'s Figure 14 data. In addition, in Figure 8, we have graphed the survival distributions for the transformed mixed gamma densities given by (7.4). The transformed distributions are gammas with shape parameters equal to 2 while the fitted gammas have shape parameters approximately equal to 1. These fitted gammas are not discernible from the transformed gamma.

In Figures 9 and 10, the VBD survival functions and boxplots for series circuits of size  $k = 2, 3, 4$  and 5 for capacitors with  $EOT = 1.4$  nm and area  $1.6 \times 10^{-5} \text{ cm}^2$ . Similar figures are given in the supplementary material for  $EOT = 1.4$  nm capacitors and area  $0.1 \times 10^{-5} \text{ cm}^2$  and  $EOT = 2.5$  nm capacitors and areas  $0.1 \times 10^{-5} \text{ cm}^2$  and  $1.6 \times 10^{-5} \text{ cm}^2$ . The boxplots are of the VBD voltage given the number of components that precipitated the series failure. The boxplots in Figure 10 are for simulations of size 40,000. The MLE's of the shape and scale are given, in Table 4, for gammas of the transformed data as are the number of capacitors that precipitate the Phase II failures of the remaining working capacitors and cause series failure.

Notice that the shape parameter of the fitted gammas are all  $\approx 1$  and the scale parameter  $\approx k$ . This is especially misleading if one is interested in the minimum extreme value for minimums of BD voltages for such series circuits. In particular, the asymptotic distribution of the minimum is a Weibull with shape parameter  $k\rho$  (not equal to  $1 \times \rho$  where  $k$  is the number of capacitors in the series circuit and  $\rho$  is the shape parameter of the capacitor VBD distribution (see discussion regarding formula (7.5)). This is further discussed in the next section on parallel/series circuits.

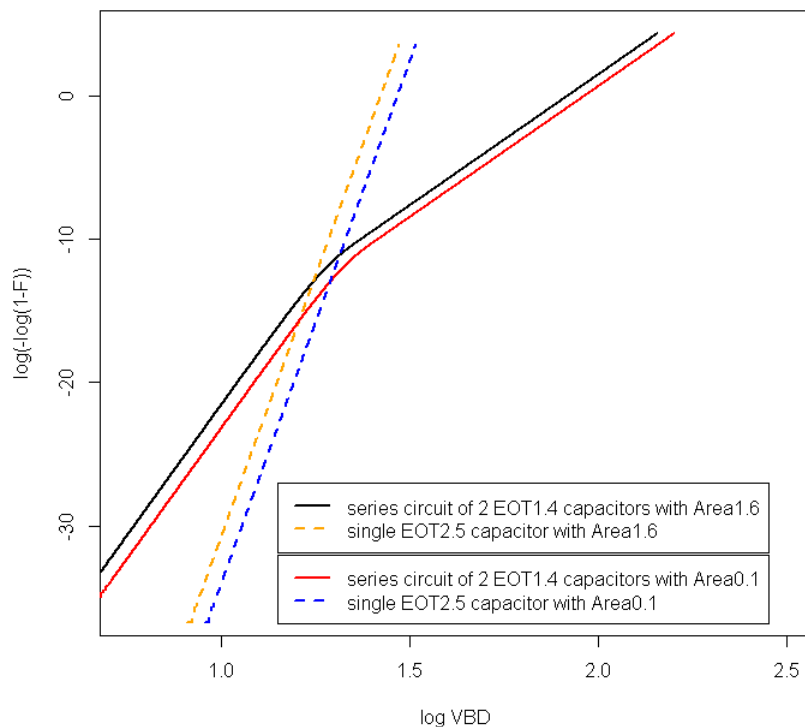


FIG 7. Weibull plots of VBD of series circuits composed of two EOT = 1.4 nm capacitors with two different oxide areas along with the VBD of their respective single EOT = 2.5 nm capacitors

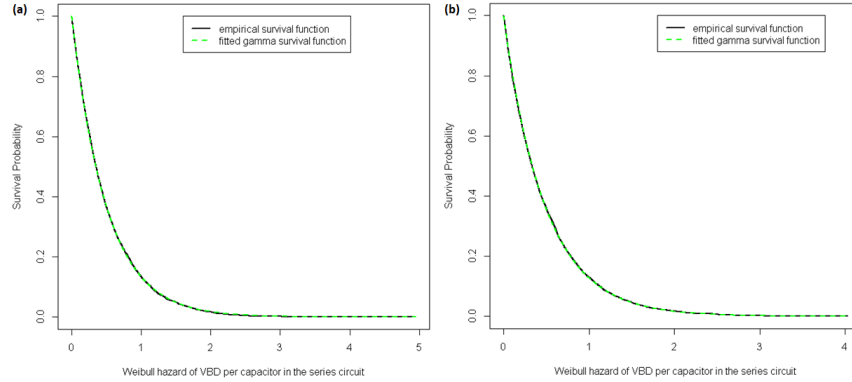


FIG 8. The survival functions of Weibull hazard of VBD of a series circuit of 2 EOT = 1.4 nm capacitors: (a) Area =  $1.6 \text{ cm}^2$  - The number of capacitor failures for the series circuit to fail was found to be 1 with probability 1. The fitted gamma distribution (in green) has the shape 1.0149 and the scale 2.0366; (b) Area =  $0.1 \text{ cm}^2$  - The number of capacitor failures for the series circuit to fail was found to be 1 with probability 1. The fitted gamma distribution (in green) has the shape 0.9951 and the scale 2.0484.

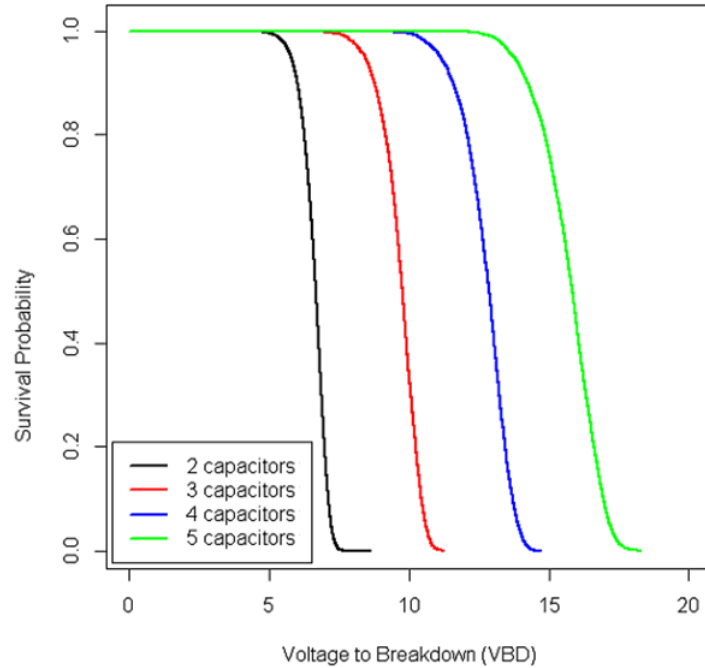


FIG 9. The survival distributions of VBD for series circuits of  $k$  capacitors,  $k = 2, 3, 4$ , and 5 with EOT = 1.4 nm, Area =  $1.6 \times 10^{-5} \text{ cm}^2$

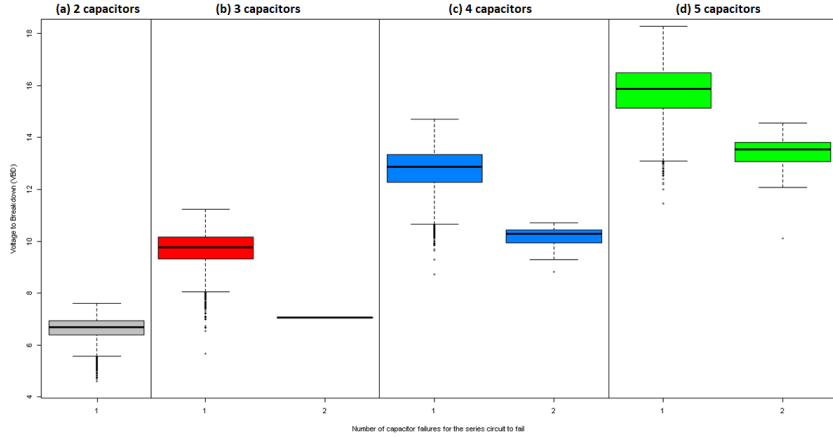


FIG 10. Boxplots of VBD given the number of failures that precipitate failure for series circuits of  $k$  capacitors,  $k = 2, 3, 4$ , and 5 with  $EOT = 1.4 \text{ nm}$ ,  $\text{Area} = 1.6 \times 10^{-5} \text{ cm}^2$

TABLE 4  
Fitted transformed gamma for series circuits of  $k$  capacitors,  $k = 2, 3, 4$ , and 5. Estimated parameters and number of capacitors that precipitate circuit failure with  $EOT = 1.4 \text{ nm}$ ,  $\text{Area} = 1.6 \text{ cm}^2$

$k$	Shape	Scale	Number 1	Number 2
2	1.0149 ( $\approx 1$ )	2.0366 ( $\approx 2$ )	100.000%	
3	1.0074 ( $\approx 1$ )	2.9907 ( $\approx 3$ )	99.975%	0.025%
4	1.0646 ( $\approx 1$ )	4.1741 ( $\approx 4$ )	99.325%	0.675%
5	1.0270 ( $\approx 1$ )	5.1775 ( $\approx 5$ )	97.875%	2.125%

Notice that the physical thickness of an  $EOT = 2.5 \text{ nm}$  capacitor is about double that of an  $EOT = 1.4 \text{ nm}$  capacitor (9.65 nm to 4.9 nm). Consequently, a series circuit of two  $EOT = 1.4 \text{ nm}$  has roughly the same capacitance as that of an  $EOT = 2.5 \text{ nm}$  but the Weibull plots in Figure 7 indicate their BD statistical behavior is quite different.

We now compare a series circuit of  $16 \times 0.1 \times 10^{-5} \text{ cm}^2$  area capacitors with  $EOT = 1.4 \text{ nm}$  and  $2.5 \text{ nm}$  to a single  $0.1 \times 10^{-5} \text{ cm}^2$  area with the same EOT. Since a capacitor failure in a series circuit changes the capacitance but the circuit need not fail, we compare the single VBD survival distribution with a  $k$ -out-16 system where  $k$  failures cause the circuit to fail. These are done in Figures 11 and 12 which show that the survival distributions are increasingly ordered as  $k$  increases and that the single capacitor VBD survival distribution is less reliable than all the other  $k$ -out-16 system for all  $k$  when  $EOT = 2.5 \text{ nm}$  while the comparison is less clear when  $EOT = 1.4 \text{ nm}$ .

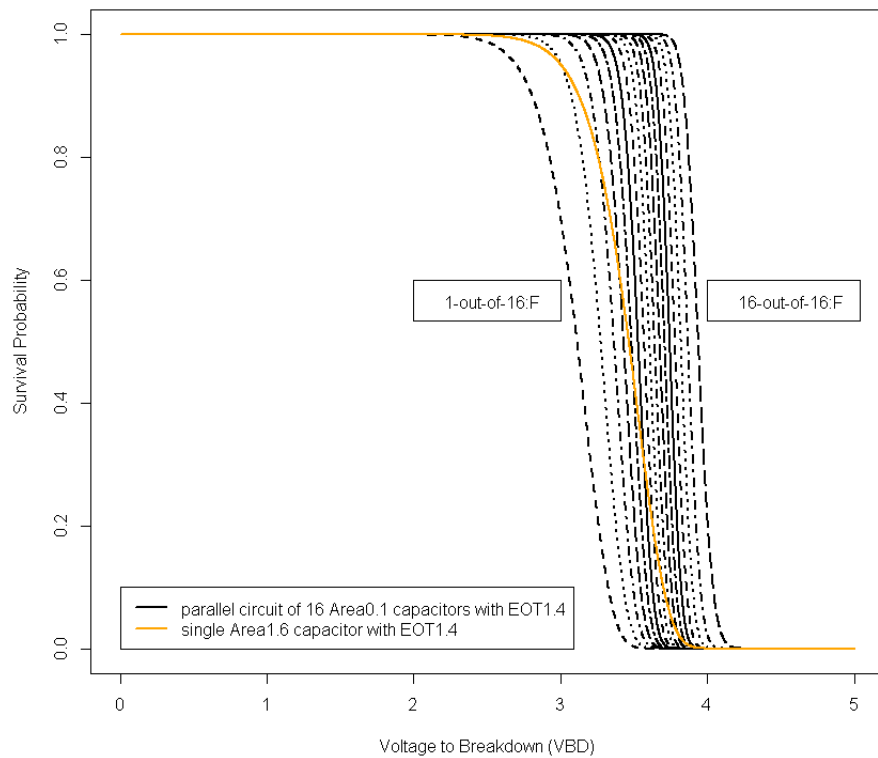


FIG 11. The survival functions of VBD of parallel circuits composed of 16 capacitors, each with  $Area = 0.1 \times 10^{-5} \text{ cm}^2$ , and a single capacitor with  $Area = 1.6 \times 10^{-5} \text{ cm}^2$  ( $EOT = 1.4 \text{ nm}$  for all these circuits)

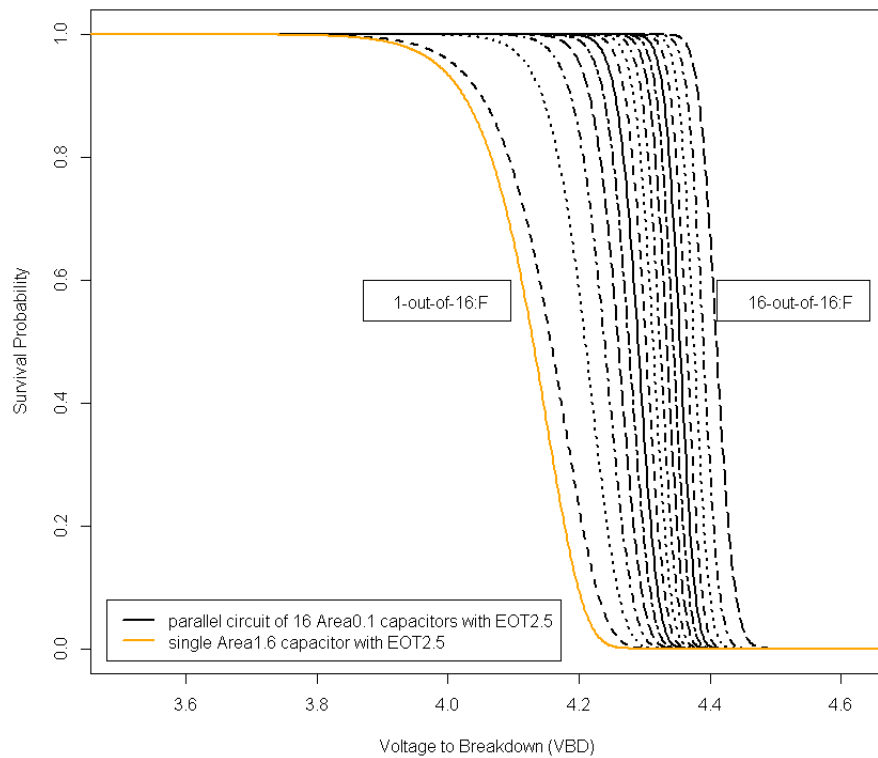


FIG 12. The survival functions of VBD of parallel circuits composed of 16 capacitors, each with  $\text{Area} = 0.1 \times 10^{-5} \text{ cm}^2$ , and a single capacitor with  $\text{Area} = 1.6 \times 10^{-5} \text{ cm}^2$  (EOT = 2.5 nm, for all these circuits)

### 9.2. Parallel/Series Circuits Based on [Kim and Lee \(2004\)](#)'s Figure 6 Data

In this section, we consider the simulation size effects for series and parallel/series circuits based on the BD distributions for [Kim and Lee \(2004\)](#)'s Figure 6 data. In Figures 13a, b, c, exact Weibull plots are given for the VBD distributions of series circuits consisting of  $k = 2, 3$  and  $4$  of  $EOT = 1.4 \text{ nm}$  and area  $0.1 \times 10^{-5} \text{ cm}^2$  capacitors as well as Weibull plots for simulations of size 100,000, 1 million and 10 million for these circuits. These plots indicate that the lower tail in the three series circuits do not stabilize until the simulation size is 1 million for circuits of size 3 and 4 and 10 million for a circuit of size 2. Table 5 gives information on the simulation size effect with regards to the lower tail; that is, the number of capacitor failures that initiate the final Phase II cycle of failures. The boxplots in Figure 14 show that at most 2 capacitors failures cause circuit failure.

TABLE 5

*The simulation-based proportions of the number of failures that precipitate failure for series circuits of  $k$  capacitors,  $k = 2, 3$ , and  $4$  with  $EOT = 1.4 \text{ nm}$  and  $\text{Area} = 0.1 \text{ cm}^2$*

No. of capacitor failures for the series circuit to fail	100,000		1,000,000		10,000,000	
	1	2	1	2	1	2
$k = 2$	0.99998	0.00002	0.999991	0.000009	0.9999941	0.0000059
$k = 3$	0.99900	0.00100	0.999066	0.000934	0.9990939	0.0009061
$k = 4$	0.99295	0.00705	0.992968	0.007032	0.9929901	0.0070099

Weibull plots are given in Figures 15 a, b, c of the VBD for parallel/series circuits where the series circuits are of size  $k = 2, 3$  and  $4$  and there are  $n = 1, 400, 40,000$ , and  $4,000,000$  series circuits are in parallel. These plots document the statistical size effect for the Weibull extreme value asymptotics. Notice that Weibull asymptotic minimum extreme value distribution is only marginally apparent for  $n = 4$  million and  $k = 3$  and  $4$  and for  $k = 2$  there is considerable curvature. Also, note that the lower tails in the Weibull plots are picking up on the Weibull asymptotics.

### 9.3. TBD and CTBD of Series Circuits

Here, we describe how the reliability of a series circuit is determined for TBD or CTBD from BD information for the capacitors. Consider a series circuit of  $N_0$  capacitors For TBD and CTBD. Here, we have Phase I failures that are due to fatiguing or wear over time. Initially, the series circuit is under a constant voltage or voltage amplitude, say  $V$ , and the time of the Phase I failure is the minimum of the failure times of the capacitors, i.e., the minimum of  $N_0$  Weibulls with shape  $\rho$  and scale  $\tau(V)$ .

At the failure of the first Phase I failure, there is a cascade of Phase II failures of the remaining working capacitors due to increased voltage or voltage amplitude due to load transfer. The number of Phase II failures is governed by the Gibbs measure (7.6) where the load per capacitor is  $N_0 V / (N_0 - 1)$  which

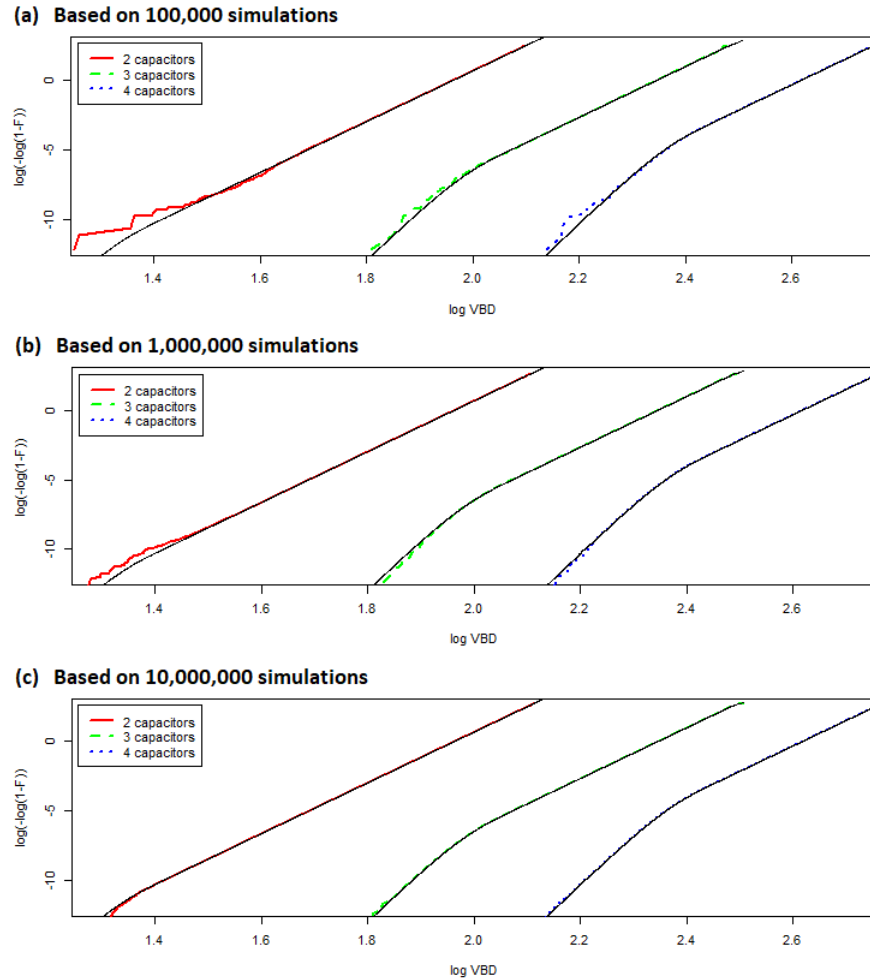


FIG 13. Weibull plots of VBD for series circuits of  $k$  capacitors,  $k = 2, 3$ , and 4 with  $EOT = 1.4 \text{ nm}$  and  $\text{Area} = 0.1 \times 10^{-5} \text{ cm}^2$ . Solid lines are exact Weibull plots

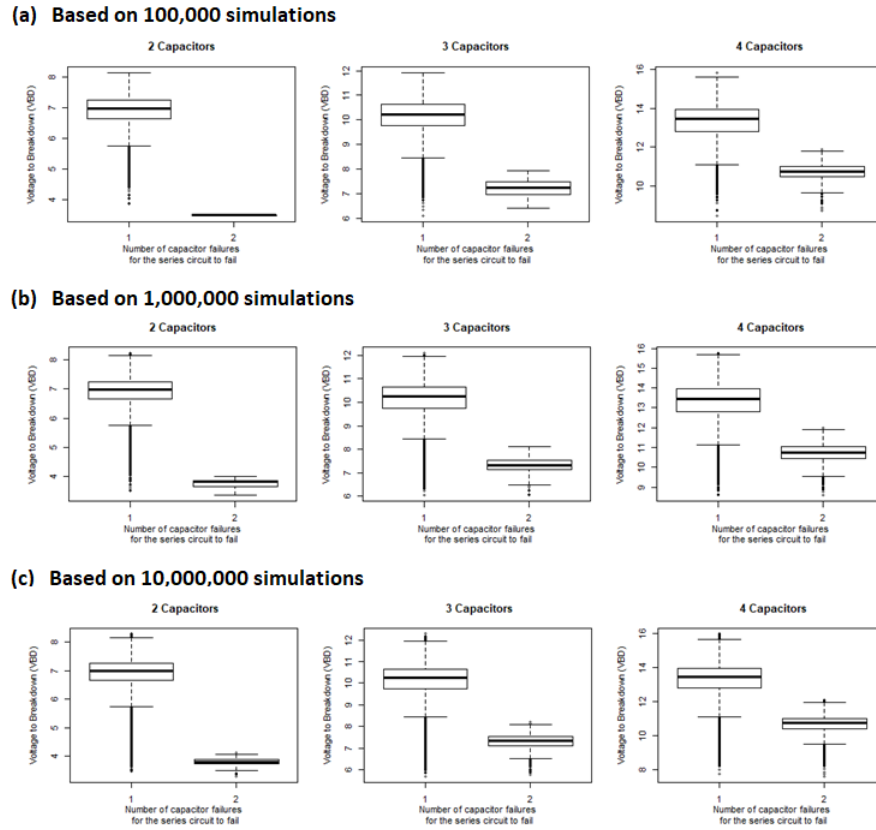


FIG 14. Boxplots of VBD given the number of failures that precipitate failure for series circuits of  $k$  capacitors,  $k = 2, 3$ , and  $4$  with  $EOT = 1.4$  nm and  $Area = 0.1 \times 10^{-5}$  cm $^2$

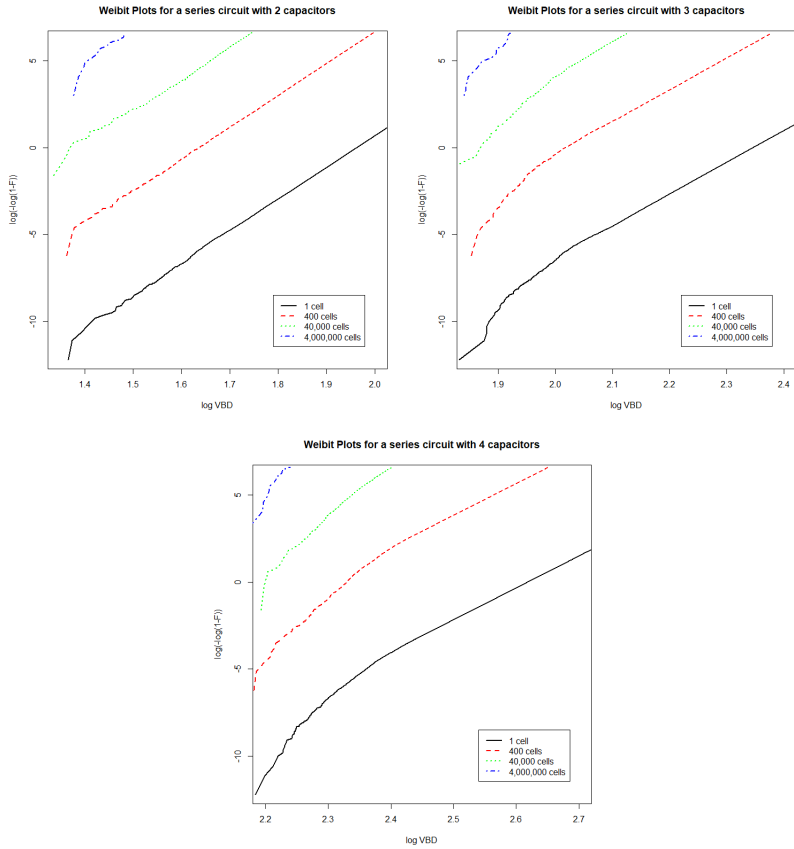


FIG 15. Weibull plots of simulated VBD among parallel/series circuits composed of different number of cells with EOT = 1.4 nm and Area =  $0.1 \times 10^{-5} \text{ cm}^2$

has to be adjusted for the number of working capacitors after this Phase I failure and the log odds that define the Gibbs measure are based on the VBD distribution of the capacitors. Incorporating the conditional information that the surviving capacitors when the Phase I failure occurs have a VBD greater than  $V$  is straightforward since the log-odds (7.7) and conditional log odds are the same in the presence of this conditioning. (See also Example (i & ii) where the Gibbs measure is specialized to the equal load-sharing rule and the Weibull distribution.)

After the first Phase I/II cycle, there remains  $N_1$  working capacitors. The voltage or voltage amplitude per the remaining number of components has increased and is  $N_0V/N_1$ . Because of the power law, this increase is reflected in the scale parameter of the Weibull failure rate for the  $N_1$  working capacitors, it is now  $\tau(NV/N_1)$  while the shape parameter does not change.

If the circuit has not failed, then you consider the next Phase I/II cycle and repeat the arguments in the preceding two paragraphs with  $N_0$  replaced by  $N_1$  and  $N_1$  replaced by  $N_2$ , the number of capacitors that survive the second Phase I/II cycle. If the circuit has not failed, repeat this recursive argument until circuit failure.

Note that the above recursive argument depends on knowing the function  $\tau(\cdot)$ . If the BD Formalism applies, then, from Consequences of A.2 & 3 (ii) of the formalism,  $\tau(V)$  is a linear function of  $\log(V)$ . For example, such a relationship is given in Figure 6, based on [Kim and Lee \(2004\)](#)'s Figure 3 HBD and SBD data.

## 10. Size Effects Relationships Motivated by the Load-Sharing Cell Model: [Kim and Lee \(2004\)](#)'s Figure 14 Data

In this section, we discuss the load-sharing (LS) cell model ([Le, Bažant and Bazant, 2009](#); [Le, 2012](#); [Bažant and Le, 2017](#)) and size effects ([Le, 2012](#), Figures 4 and 5) raised regarding [Kim and Lee \(2004\)](#) Figure 14 data. The data in Figure 14 is generated from static loading tests where three different protocols are considered. Here, the cycle time to failure is from an accelerated failure time (AFT) perspective where the load-sharing directly reduces the cycle lifetime. That is, the role of increased voltage to voltage BD is functionally replaced by increased time or number of cycles to cycle breakdown.

In the next subsection, we discuss further background regarding Kim and Lee's data, size effects, and the load-sharing cell model. This is followed by a subsection where simulations based on this data are used to illustrate size effects.

### 10.1. Background

Our earlier analysis of the [Kim and Lee \(2004\)](#)'s Figure 14 data was given in Section 8.1 where

- (i) the Weibull was not refuted as a model for the CTBD data,

- (ii) the curvature emphasized in [Le \(2012\)](#)'s Figure 4 Weibull plots is not discernable from background variation in our Figure 2, but
- (iii) the Weibull plots of the lognormal, the log-logistic and the Birnbaum-Saunders fits in Figure 1 accentuate the curvature.<sup>4</sup>

The Weibull plots for this data are given in Figure 16 below, but where the shape parameter is the same for all three protocols. The plots support the BD formalism regarding static CTBD where the shape is the same when the cycle voltage amplitude is the same but differences in the protocol for the on/off cycle length and the frequencies affect the scale parameter.

In this model, a cell consists of a series circuit of nano-capacitors (subcells) where, as subcells fail, the voltage (amplitude since we consider static cyclic loading under different testing protocols) load is distributed equally to the surviving subcells. How faithful this model is to the actual physics of a dielectric cell BD is not clear given the quantum effects that govern its behavior. A modification of their cell model is discussed, below, that addresses some of this.

[Le \(2012\)](#) and [Bažant and Le \(2017\)](#) discussed size effects for the LS cell model like those considered in Sections 9.1 and 9.2 for parallel/series circuits of ordinary capacitors. Here, the dielectric is viewed as a parallel circuit of cells where the number of cells is proportional to the cross-sectional area of the dielectric and the thickness of the dielectric determines the number of subcells in a cell. They distinguished the *weakest link model* from the *finite weakest link model*, where the former is an infinitely long parallel circuit and the minimum extreme value asymptotics lead to the BD distribution being Weibull. [Le \(2012\)](#) used what he called a grafted distribution (see [Le \(2012\)](#), formulas (17)–(18) or [Bažant and Le \(2017\)](#), formulas (14.8)–(14.9)) for the BD cycle time for a cell and used it as the reference distribution to quantify the size effects between the BD distributions for the two models (see Figure 5 of [Le \(2012\)](#), or Figure 14.9 of [Bažant and Le \(2017\)](#)).

As mentioned in Section 4, such size effects were considered earlier. Of particular note for this section is [Taylor \(1987\)](#)'s work on the static fatigue of semicrystalline polymer materials. There the polymer is modeled as a weakest link chain-of-bundles model. Defects occur in the amorphous regions in a bundle where cracks are initiated in the polymer material at random times. A pure birth process models the crack growth of a particular crack where the times between births have exponential distributions with birth rates based on stress factors at the boundary of the crack. These are explosive birth processes; there is an infinite number of births in finite time which is referred to as the *explosion time*. The time it takes for a given crack to cause bundle failure is the sum of

---

<sup>4</sup>Such curvature is very apparent in the raw Weibull plots given in Figure 5 of [Ntenga et al. \(2019\)](#). These plots are for the tensile strength of plant fibers (PFs). The authors use a Weibull in their analysis even though they note that a lognormal has a better fit due to this curvature. However, “PF properties are considerably influenced by their hierarchic composite microstructure” which consists of “cellulose microfibrils about the axis of the fiber.” This suggests that a chain-of-bundles may be an appropriate model for the PF and that the curvature could be due to a finite weakest link size effect discussed earlier in Section 4 and later, below.

the time it takes the defect to initiate crack growth plus its explosion time. The polymer failure time is the minimum of the bundle failure times. [Taylor \(1987\)](#) used this formulation to construct what he calls the *characteristic distribution function*, which has the *exact weakest link relationship*, and uses it as a reference distribution to study the size effect (see [Taylor \(1987\)](#)'s formulas (5.4)–(5.9)).

As indicated in Sections 3.3 and 3.4, the breakdown mechanisms are very different for  $\text{SiO}_2$  dielectrics v.  $\text{HfO}_2$  dielectrics. In the former, complete percolation paths form and disperse under the influence of the electric field, leading to repeated SBDs. The concurrent physical changes in the dielectric are reversible until the local temperature along a complete path remains high enough for a time that is long enough to melt an ohmic conduction path through the dielectric, producing a HBD. Notice that the times of  $\text{SiO}_2$  SBDs of the dielectric behave like Weibulls (see [Kim and Lee \(2004\)](#), Figure 3 and [Strong et al. \(2009\)](#), Figure 3.81) where the shape parameter of the  $k$ th SBD Weibull increases to that of the HBD shape parameter. Unfortunately, it is not clear how this can be used to model the SBD time of a cell that initiates irreversible damage that leads to failure of the cell.

On the other hand, for the latter, the leakage current leads to irreversible damage, due to the physical structure of the dielectric, with crystal grains separated by amorphous GBs containing the defects (trapping sites). [Taylor \(1987\)](#)'s approach suggested the following modification that makes it more faithful to the physics of dielectric BD as described in Section 3.5. Dielectric BD initiates in the grain boundary where electron trapping/detrapping increases local vibrational and temperature effects. These change the structure of the GB and create a feedback loop that increases the leakage current. At some point, the capacitor discharges through the GB (a SBD); the charge must then rebuild, leading to further SBDs. Eventually, the local temperature along with the GB remains high enough for a time long enough to melt an ohmic conduction path along the GB, which concurrently expands somewhat into the adjacent grains. The times between the breakdown events may be viewed as a birth process.

[Taylor \(1987\)](#) considered a chain-of-bundles/weakest link model for a polymer. A “spatial” Poisson process in the  $(t, y)$  plane where the rate of the Poisson at  $(t, y)$  is  $vf(y)$ ;  $v$  is the rate of occurrence of a defect that appears through time and  $f(y)$  is the density of the explosion times. Here,  $v$  depends on the size of the bundle and on the load on the bundle. To emulate Taylor, though, would be more complicated since the rate  $v$  and  $f$  would depend on the coarseness of the anode interface.

As indicated in Section 3, other modifications need to be made to account for information regarding the coarseness of the  $\text{HfO}_2$  metal interface with the anode and for the percentage of the dielectric that is grain boundary. [Pirrotta et al. \(2013\)](#) discussed the roles of the grains and grain boundaries in the conduction of electrons through the dielectric while [Zhang et al. \(2019\)](#) indicated how the coarseness depends on the annealing temperature. Figure 1 of [Zhang et al. \(2019\)](#) (see also Figure 2 of [Pirrotta et al. \(2013\)](#)) indicated how the coarseness depends on the annealing temperature. This coarseness is reflected in the peaks and valleys of the interface; the heights are different where the valleys/“deeper paths

that correspond to the grain boundaries.” The asymptotic survival distribution for the minimum CTBD time for a given height is Weibull where the shape parameter,  $\beta$ , is proportional to its height.

The distribution of bundle sizes of the grain boundary structure can be incorporated by mixing over  $\beta$  where the mixing proportions are determined by the fraction of the grain boundary sizes in these peaks and valleys. The scale parameter,  $\tau$ , is more problematic but one could imagine that its relationship voltage,  $V$ , is that  $\log \tau$  is linear in  $\log V$  for a static load  $V$ . Determining good models for the joint behavior of  $(\tau, \beta)$  is an open question but would give ways to realistically model the BD distribution of such  $\text{HfO}_2$  dielectrics as a (weakest-link) chain-of-bundles model.

Another possibility is to statistically model the coarseness as follows. It is clear from [Pirrotta et al. \(2013\)](#) and [Zhang et al. \(2019\)](#) that the experimentalists can extract very detailed data regarding the coarseness. If one has the data for a number of specimens, one could construct a Dirichlet/Gamma process for the heights,  $z$ , over an  $(x, y)$  grid cell where the cell and the height is based on the resolution of the measuring device. With this structure, a nonparametric posterior empirical Bayes estimator of the surface can be constructed based on the data to model the coarseness. The above approaches to modeling the coarseness are open areas of possible future research.

### 10.2. Size effect simulations

Now, we consider the load-sharing cell model and look at size effects based on subcells CTBD distributions consistent with the CTBD Weibull plots given in Figure 17. Since the lattice constant is about 1 for some types of pure  $\text{HfO}_2$  pure crystals and the physical thickness is about 5 nm for [Kim and Lee \(2004\)](#)’s data, a pure grain cell would consist of about 5 pure subcells. This is consistent with [Le \(2012\)](#)’s description of the cell size where a defect is about the size of 1 subcell.

Since the actual failure of the dielectric is initiated in the grain boundary and the Weibull plots have a shape parameter of about 3 (hence 3 subcells), this suggests that the behavior of the load-sharing distribution for a grain boundary cell at the origin can be approximated by a mixture of gammas with shape parameter 3. Hence, subcell CTBD times are assumed to be i.i.d. exponential in the discussion of cell BD and size effects for dielectric breakdown given, below. In addition, the length of the chain reflects the amount of the grain boundary that makes up the cross-sectional area of the dielectric.

Furthermore, unit exponentials (scale parameter equals 1) are chosen in the computations, since the analysis for an arbitrary scale parameter can be easily adjusted in the analysis. (Daniels equal load-sharing rule justifies this; multiply the unit exponential time to failure of a subcell by the characteristic lifetime/scale parameter for a subcell. Also, the BD distributions for the 3 different cycles to failure protocols is just a scale change so it can be adjusted in the same way.) With this choice of the subcell BD cycle times and with the equal load-sharing rule for the cell, we investigate the size effects for this model. This

investigation is similar to the one in Sections 9.1 and 9.2, where series circuits of size, 2, 3, 4 and 5, were considered, except that the subcell BD distributions, here, are compatible with Figure 16 information.

Figures 17–22 and Tables 6 and 7 indicate simulation size effects for series circuits of capacitors of size  $k = 2, 3, 4$  and 5 and the cycle time to breakdown (CTBD) distribution of the capacitors is unit exponential. Figures 17 and 18 give the exact Weibull plots and survival distributions for these series circuits based on formula (7.4) since the capacitors CTBD distribution is unit exponential. Notice that the curvature in the Weibull plots increases as  $k$  increases where the slope of the plots at the right end of the plot is around 2 and at the left end is  $k$  for the series circuit of  $k$  capacitors.

Based on simulations of size 100,000, the boxplots, given the number of capacitors failures that precipitate circuit failure for a series circuit of size  $k$ ,  $N_k$ , in Figure 19 for CTBD are very similar. Thus, there is very little information on the number of capacitor failures prior to circuit failure in predicting circuit failure. Information, based on simulations of size 100,000, about the distribution of the  $N_k$  are given in Table 6. Also, note that MLE fitted gammas have shape parameters that are related to the circuit size.

Figure 20 indicates the simulation size effect in the Weibull plots simulations of size 10, 1000, and 100,000 for the four different circuit sizes. Table 7 and Figure 21 gives information regarding these simulations of the distribution of  $N_k$ . These indicate just how well the simulation size affects the Weibull plots and the estimates of the distributions. Finally, the boxplots in Figure 22 illustrates the simulation size effects for the conditional distribution of the CTBD given  $N_k$ .

Figure 23 gives part of the exact Weibull plots for parallel/series circuits of capacitors with unit exponential CTBD distributions. Let  $\bar{F}_k(t)$  denote the CTBD survival distribution of a series circuit of size  $k$ . Then, a parallel circuit of  $n$  series circuits of size  $k$  has CTBD survival distribution  $\bar{F}_{k,n}(t) \equiv [\bar{F}_k(t)]^n$ . Thus, the  $y$ -coordinate of the Weibull plot of  $\bar{F}_{k,n}(t)$  is

$$\log[\log(\bar{F}_{k,n}(t))] = \log n + \log[-\log(\bar{F}_k(t))]$$

which is a vertical shift of  $\log(-\log(\bar{F}_k(t)))$  at  $\log t$ .

Figure 23 gives insights into the size effects due to size of the parallel circuit. From Figure 23a, the curvature in the plots is around  $\log \text{CTBD} = 0$  or  $\text{CTBD} = 1$ . Since  $0 \approx \bar{F}_{2,n}(1)$  for  $n = 40,000$  and  $4,000,000$ , the Weibull asymptotics are appropriate for these values of  $k$  but a finite weakest link adjustment is necessary for  $n = 400$  for the right tail of  $\bar{F}_{2,400}$ . Similar statements can be made regarding circuits of size  $k = 3, 4$  and 5.

The above shows how to assess the size effect for the load-sharing cell model where a cell is a series circuit of  $k$  capacitors with unit exponential CTBD. As mentioned earlier, to account for the coarseness of the interface surface at the metal anode end of  $\text{HfO}_2$  dielectrics, one can mix over  $k$  where the mixing proportions are determined by the coarseness. Also, the size of the parallel circuit is determined by the percentage of the dielectric's grain boundary.

Kim and Lee's Figure 14: Weibull probability plots with 95% CIs

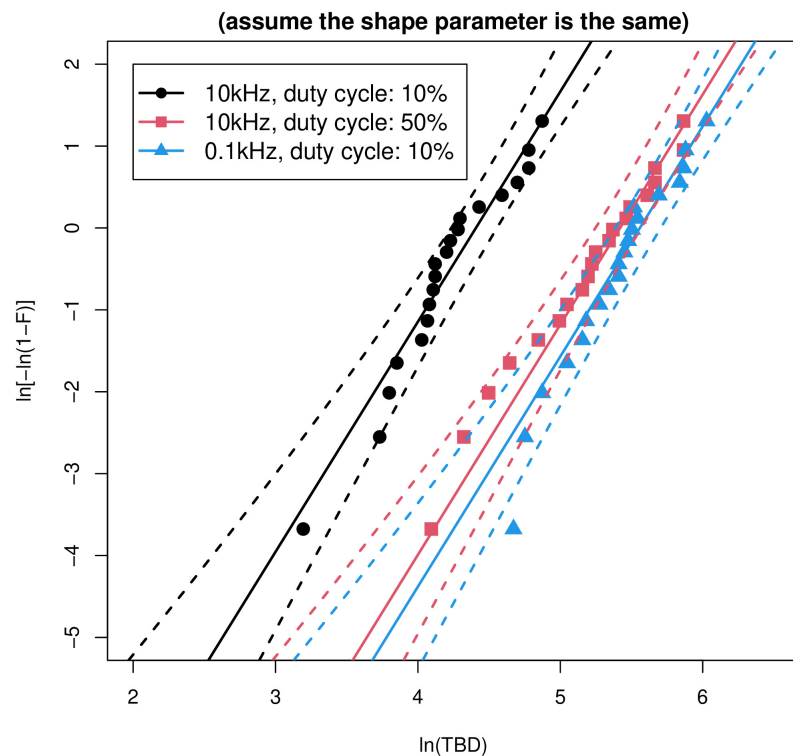


FIG 16. Weibull plots of [Kim and Lee \(2004\)](#)'s Figure 14 data with the same shape parameter = 2.810153; (a) 10kHz, 10% duty cycle: scale parameter = 4.407255; (b) 10kHz, 50% duty cycle: scale parameter = 5.420054; (c) 0.1kHz, 10% duty cycle: scale parameter = 5.558458

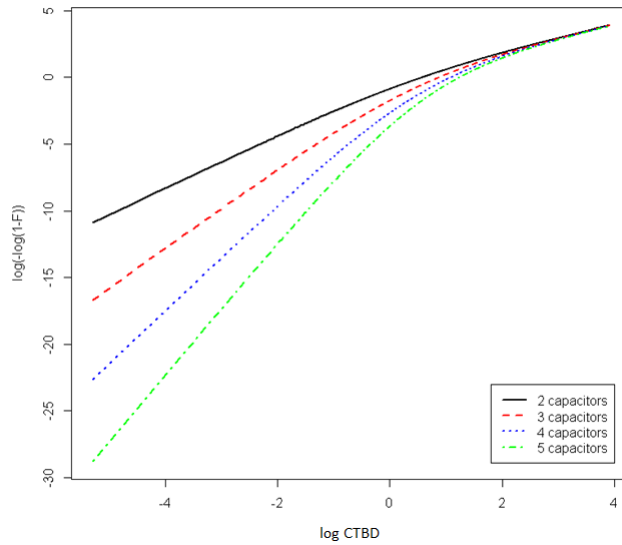


FIG 17. Weibull plots for CTBD for series circuits with  $k$  capacitors,  $k = 2, 3, 4, 5$ . Capacitors CTBD distribution is the unit exponential distribution.

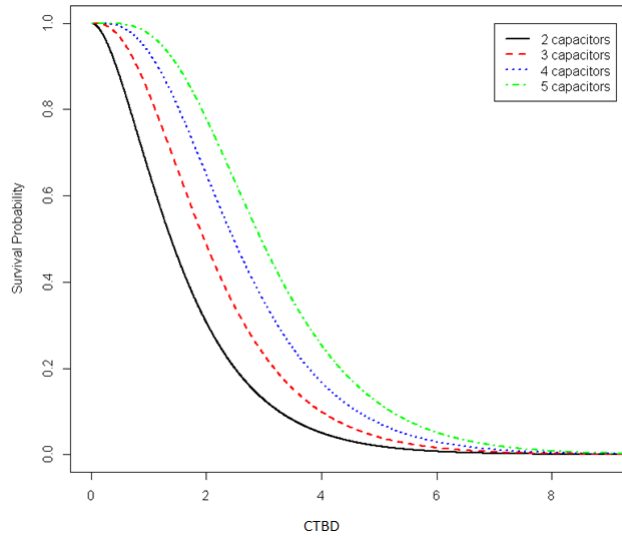


FIG 18. The survival distributions of CTBD for series circuits with  $k$  capacitors,  $k = 2, 3, 4, 5$ . Capacitors CTBD distribution is the unit exponential distribution.

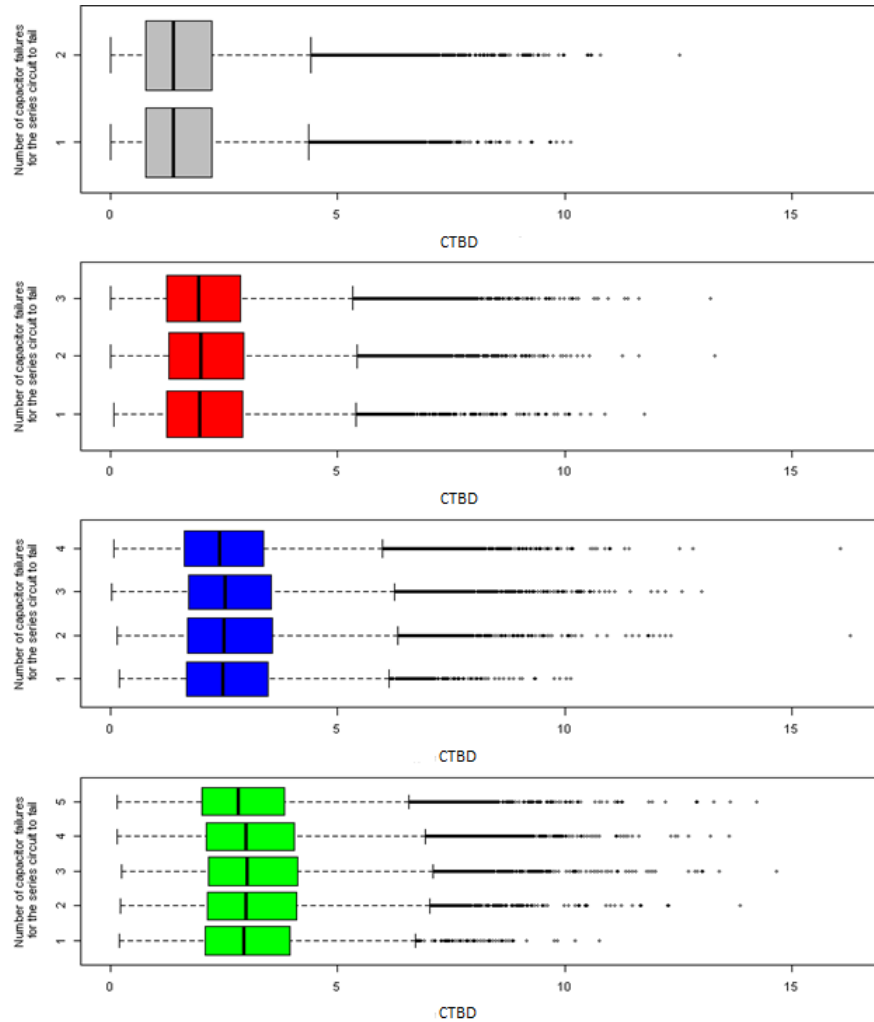


FIG 19. Boxplots of CTBD given the number of capacitor failures that precipitate circuit breakdown for series circuits with  $k$  capacitors,  $k = 2, 3, 4, 5$ . Based on simulations of size 100,000.

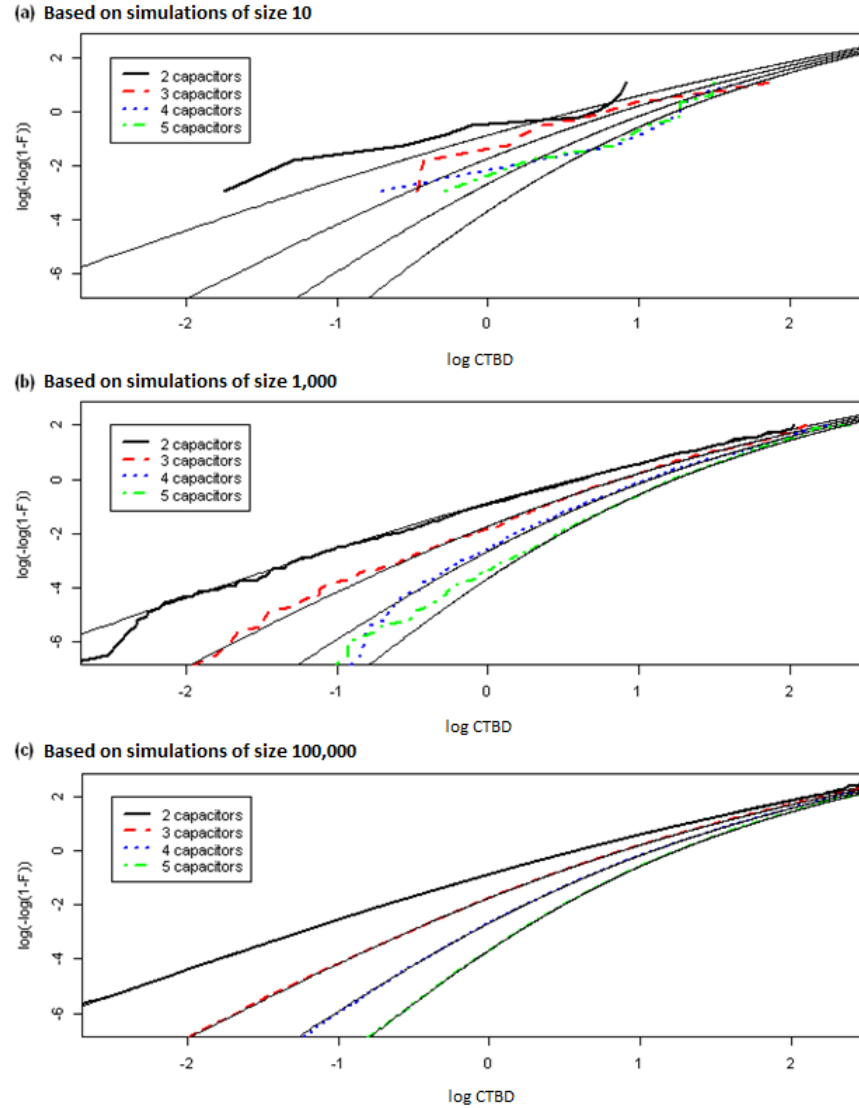


FIG 20. Weibull plots of CTBD for series circuits with  $k$  capacitors,  $k = 2, 3, 4, 5$ . Based on simulations of size 10, 1000, and 100,000.

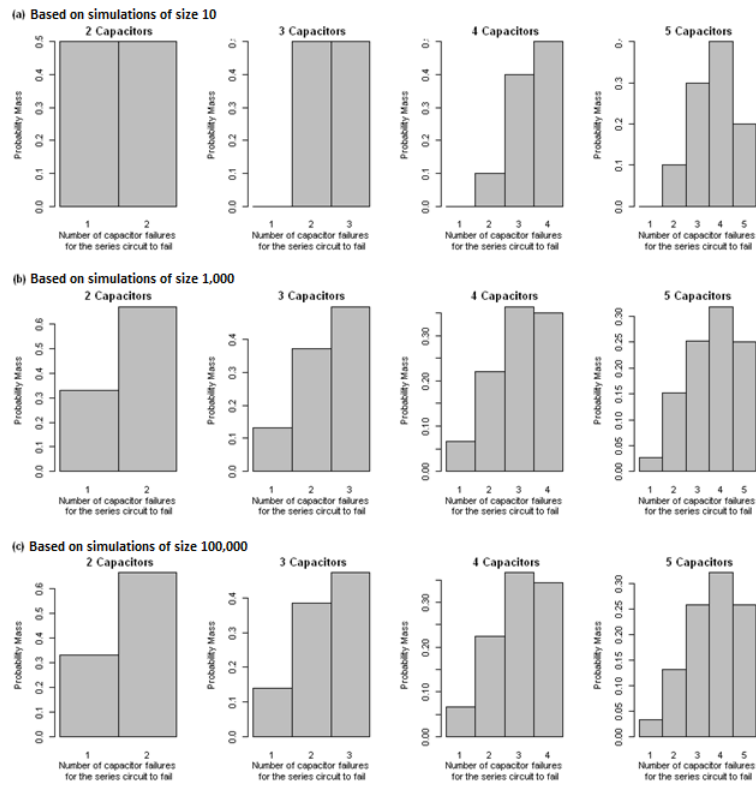


FIG 21. Histograms for the number of capacitor failures that precipitate circuit breakdown for series circuits with  $k$  capacitors,  $k = 2, 3, 4, 5$ . Based on simulations of size 10, 1000, and 100,000.

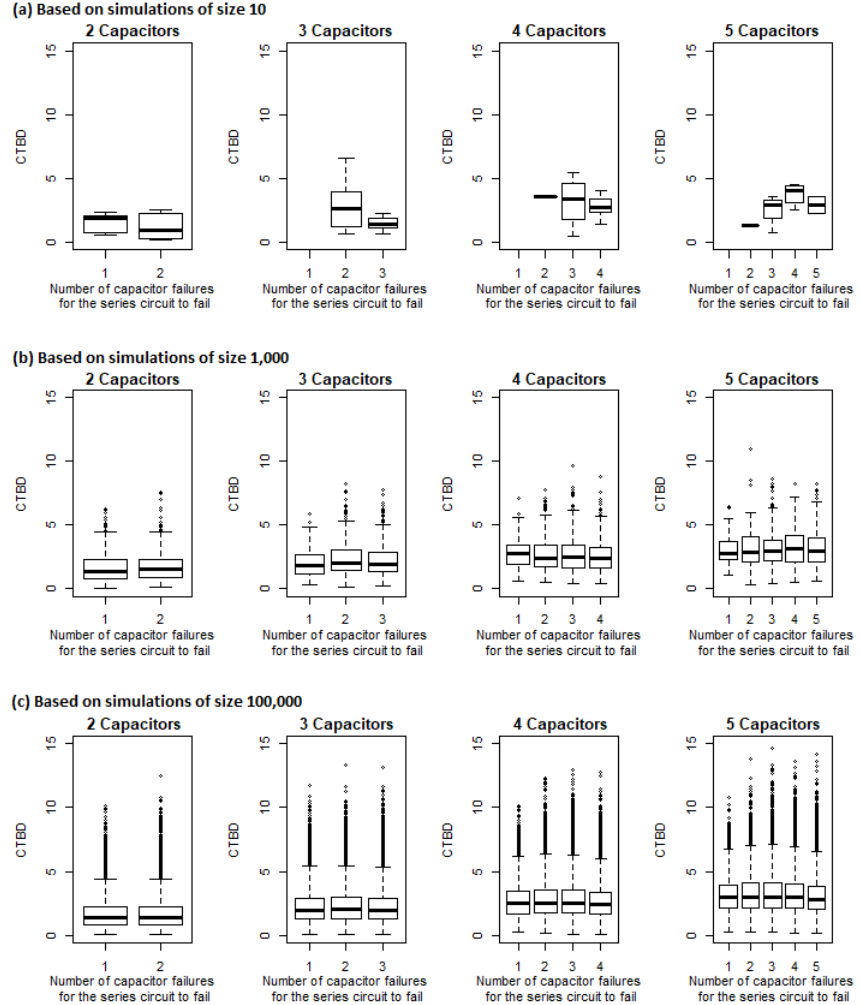


FIG 22. Boxplots of  $CTBD$  given the number of capacitor failures that precipitate circuit breakdown for series circuits with  $k$  capacitors,  $k = 2, 3, 4, 5$ . Based on simulations of size 10, 1000, and 100,000.

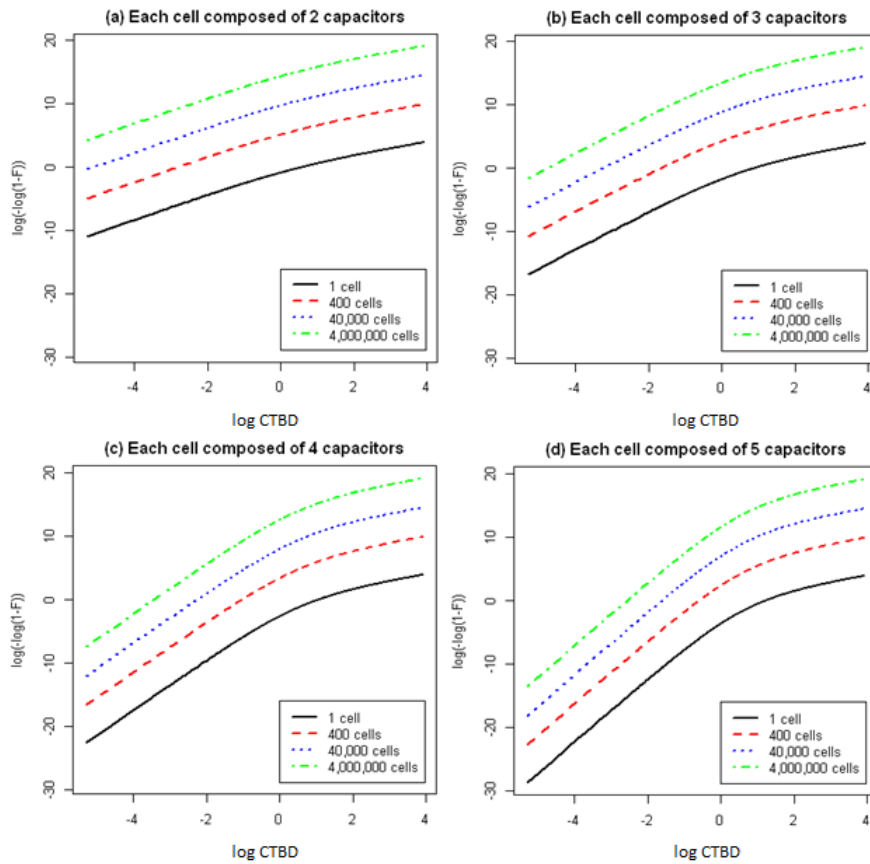


FIG 23. Weibull plots of CTBD among parallel/series circuits composed of different number of cells. Each cell is composed of different number of capacitors where the capacitor CTBD distribution is the unit exponential distribution.

TABLE 6

*Estimated probabilities for the number of capacitor failures that precipitate circuit breakdown for series circuits with  $k$  capacitors,  $k = 2, 3, 4, 5$ . Based on simulations of size 100,000. MLEs are for the gamma parameters fit.*

Number of Capacitors	Number of capacitor failures for the series circuit to fail					Gamma Scale	Parameter Shape	MLE
	1	2	3	4	5			
2	0.33240	0.66760	—	—	—	2.3566	1.9620 ( $\approx 2$ )	
3	0.14058	0.38581	0.47361	—	—	3.8881	2.8824 ( $\approx 3$ )	
4	0.06584	0.22308	0.36679	0.34429	—	5.4926	3.7426 ( $\approx 4$ )	
5	0.03276	0.13083	0.25729	0.32117	0.25795	7.2019	4.6004 ( $\approx 5$ )	

TABLE 7

*Estimated probabilities for the number of capacitor failures that precipitate circuit breakdown for series circuits with  $k$  capacitors,  $k = 2, 3, 4, 5$ . Based on simulations of size 10, 1000, and 100,000.*

Simulation Size	Number of Capacitors	Number of capacitor failures for the series circuit to fail				
		1	2	3	4	5
10	2	0.5	0.5	—	—	—
	3	0.0	0.5	0.5	—	—
	4	0.0	0.1	0.4	0.5	—
	5	0.0	0.1	0.3	0.4	0.2
1,000	2	0.331	0.669	—	—	—
	3	0.133	0.370	0.497	—	—
	4	0.067	0.220	0.363	0.350	—
	5	0.027	0.152	0.252	0.318	0.251
100,000	2	0.33240	0.66760	—	—	—
	3	0.14058	0.38581	0.47361	—	—
	4	0.06584	0.22308	0.36679	0.34429	—
	5	0.03276	0.13083	0.25729	0.32117	0.25795

## 11. Concluding Comments

Over the last sixty years fiber bundle models (FBM) have played a fundamental role in the analysis of the reliability of certain types of complex load-sharing systems. It was first used in the study of the strength of yarns and threads followed by modeling the reliability of fibrous composites. This followed with their use in the investigation of the fracture and breakdown (BD) of disordered materials studied by material scientists. Limitless applications of the fiber bundle models can be found in the fields of material science, mechanical and structural engineering, and nanotechnology since modern disordered materials are extensively used in these areas. In addition, FBM have been used in the geosciences to understand how rapid mass movements, such as avalanches, are triggered.

Since FBM are stochastic in nature and because of their importance in the analysis of system BD, we presented an overview of the statistical FBM. Here the emphasis was on the statistical aspects to make it accessible to statistical types not familiar with the topic. This was accomplished by concentrating on both the physical and statistical aspects of a specific load-sharing example, the breakdown (BD) for circuits of capacitors and related dielectrics. For series and

parallel/series circuits (series/parallel reliability systems) of ordinary capacitors, the load-sharing rules were derived from the electrical laws. This with the BD formalism was then used to obtain the BD distribution of the circuit. The BD distribution and Gibbs measure were given for a series circuit and the size effects were illustrated for simulations of series and parallel/series circuits. This is related to the finite weakest link adjustments for the BD distribution that arise in large series/parallel reliability load-sharing systems, such as dielectric BD, from their extreme value approximations.

An elementary but in-depth discussion of the physical aspects of  $\text{SiO}_2$  and  $\text{HfO}_2$  dielectrics and cell models was given. This was used to study a load-sharing cell model for the BD of  $\text{HfO}_2$  dielectrics and the BD formalism. The latter was based [Kim and Lee \(2004\)](#)'s comprehensive study of such dielectrics and an analysis of their data. Here, several BD distributions were compared in the analysis and proportional hazard regression models were used to study the BD formalism.

Critical findings were as follows. It was discovered that for very thin dielectrics, the A.1 Weakest Link Principle, a proportional hazards model, was no longer proportional to the area but that a proportional hazard model (A.1') still obtained. Also, regression models were also used to predict HBDs based on the first SBD time. In addition, size effects were studied via simulations for the load-sharing cell model based on this data.

Some stochastic models were proposed to better account for the finite weakest link adjustments size effect adjustments and spatial models were proposed to account for information regarding the coarseness of the  $\text{HfO}_2$  metal interface with the anode and for the percentage of the dielectric that is grain boundary.

## Acknowledgement

We would like to thank David Fecko at the Pennsylvania State University's Materials Research Institute (MRI) for arranging a visit to MRI's dielectrics testing center. We would especially like to thank Eugene Furman of MRI for several insightful discussions and numerous references on dielectrics. As noted earlier, we want to thank J. C. Lee and J-L. Le for their efforts regarding the data in [Kim and Lee \(2004\)](#) and [Le \(2012\)](#).

This material was based upon work partially supported by the National Science Foundation under Grant DMS-1127914 to the Statistical and Applied Mathematical Sciences Institute (SAMSI). Any opinions, findings, and conclusions or recommendations expressed in this material are those of the authors and do not necessarily reflect the views of the National Science Foundation.

## References

ALAM, M. A., WEIR, B. E. and SILVERMAN, P. J. (2002). A study of soft and hard breakdown – Part I: Analysis of statistical percolation conductance. *IEEE Transactions on Electron Devices* **49** 232–238.

ALAM, M. A., WEIR, B., BUDE, J., SILVERMAN, P. J. and MONROE, D. (1999). Explanation of soft and hard breakdown and its consequences for area scaling. In *International Electron Devices Meeting 1999. Technical Digest (Cat. No.99CH36318)* 449–452.

BAŽANT, Z. P. and LE, J.-L. (2017). *Probabilistic Mechanics of Quasibrittle Structures – Strength, Lifetime, and Size Effect*. Cambridge University Press, Cambridge, UK.

BERSUKER, G., SIM, J. H., PARK, C. S., YOUNG, C. D., NADKARNI, S. V., CHOI, R. and LEE, B. H. (2007). Mechanism of electron trapping and characteristics of traps in  $\text{HfO}_2$  gate stacks. *IEEE Transactions on Device and Materials Reliability* **7** 138–145.

BHATTACHARYYA, P. and CHAKRABARTI, B. K. (2006). *Modelling Critical and Catastrophic Phenomena in Geoscience - A Statistical Physics Approach*. Springer, Berlin, Heidelberg.

BOUFASS, S., HADER, A., TANASEHTE, M., SBIAAI, H., ACHIK, I. and BOUGHALEB, Y. (2020). Modelling of composite materials energy by fiber bundle model. *The European Physical Journal Applied Physics* **92** 10401.

CHATTERJEE, S., KUO, Y., LU, J., TEWG, J. Y. and MAJHI, P. (2006). Electrical reliability aspects of  $\text{HfO}_2$  high- $k$  gate dielectrics with TaN metal gate electrodes under constant voltage stress. *Microelectronics Reliability* **46** 69–76.

CHU, F. (2014). A Review on Conduction Mechanisms in Dielectric Films. *Advances in Materials Science and Engineering* **2014** 578168.

COHEN, D., SCHWARZ, M. and OR, D. (2011). An analytical fiber bundle model for pullout mechanics of root bundles. *Journal of Geophysical Research: Earth Surface* **116** F03010.

DANIELS, H. E. (1945). The Statistical Theory of the Strength of Bundles of Threads. I. *Proceedings of the Royal Society of London. Series A, Mathematical and Physical Sciences* **183** 405–435.

DISSADO, L. A. and FOTHERGILL, J. C. (1992/2008). *Electrical Degradation and Breakdown in Polymers*. The Institution of Engineering and Technology, London, United Kingdom. Original work published 1992; Reprinted in 2008.

DURHAM, S. D. and LYNCH, J. D. (2000). A threshold representation for the strength distribution of a complex load sharing system. *Journal of Statistical Planning and Inference* **83** 25–46.

EBRAHIMI, N., MCCULLOUGH, K. and XIAO, Z. (2013a). Reliability of sensors based on Nanowire networks. *IIE Transactions* **45** 215–228.

EBRAHIMI, N., MCCULLOUGH, K. and XIAO, Z. (2013b). Reliability of Sensors Based on Nanowire Networks With Either an Equilateral Triangle Lattice or a Hexagonal Lattice Structure. *IEEE Transactions on Nanotechnology* **12** 81–95.

HANSEN, A., HEMMER, P. C. and PRADHAN, S. (2015). *The fiber bundle model: Modeling failure in materials*. Wiley-VCH, Weinheim, Germany.

HARLOW, D. G. and PHOENIX, S. L. (1978a). The Chain-of-Bundles Probability Model For the Strength of Fibrous Materials I: Analysis and Conjectures. *Journal of Composite Materials* **12** 195–214.

HARLOW, D. G. and PHOENIX, S. L. (1978b). The Chain-of-Bundles Probability Model for the Strength of Fibrous Materials II: A Numerical Study of Convergence. *Journal of Composite Materials* **12** 314–334.

HARLOW, D. G. and PHOENIX, S. L. (1982). Probability distributions for the strength of fibrous materials under local load sharing I: Two-level failure and edge effects. *Advances in Applied Probability* **14** 68–94.

HARLOW, D. G., SMITH, R. L. and TAYLOR, H. M. (1983). Lower Tail Analysis of the Distribution of the Strength of Load-Sharing Systems. *Journal of Applied Probability* **20** 358–367.

HOUSSA, M., STESMANS, A., NAILI, M. and HEYNS, M. M. (2000). Charge trapping in very thin high-permittivity gate dielectric layers. *Applied Physics Letters* **77** 1381–1383.

IGLESIAS, V., PORTI, M., NAFRIA, M., AYMERICH, X., DUDEK, P. and BERSUKER, G. (2011). Dielectric breakdown in polycrystalline hafnium oxide gate dielectrics investigated by conductive atomic force microscopy. *Journal of Vacuum Science Technology, B* **29** 01AB02.

JONES, E. R. (1971). *Solid State Electronics*. Intext Educational Publishers, Scranton, PA, USA.

KIM, Y.-H. and LEE, J. C. (2004). Reliability characteristics of high- $k$  dielectrics. *Microelectronics Reliability* **44** 183–193.

KITTEL, C. (2004). *Introduction to Solid State Physics, 8th Edition*. John Wiley & Sons Inc, New York, NY, USA.

KUN, F., RAISCHEL, F., HIDALGO, R. C. and HERRMANN, H. J. (2006). Extensions of Fibre Bundle Models. In *Modelling Critical and Catastrophic Phenomena in Geoscience* 57–92. Springer Berlin Heidelberg.

LE, J.-L. (2012). A finite weakest-link model of lifetime distribution of high- $k$  gate dielectrics under unipolar AC voltage stress. *Microelectronics Reliability* **52** 100–106. 2011 Reliability of Compound Semiconductors (ROCS) Workshop.

LE, J.-L., BAŽANT, Z. P. and BAZANT, M. Z. (2009). Lifetime of high- $k$  gate dielectrics and analogy with strength of quasibrittle structures. *Journal of Applied Physics* **106** 104119.

LECKEY, K., MÜLLER, C. H., SZUGAT, S. and MAURER, R. (2020). Prediction intervals for load-sharing systems in accelerated life testing. *Quality and Reliability Engineering International* **36** 1895–1915.

LEE, S., DURHAM, S. and LYNCH, J. (1995). On the calculation of the reliability of general load sharing systems. *Journal of Applied Probability* **32** 777–792.

LEE, S. J., JEON, T. S. and KWONG, D. L. (2002). Hafnium oxide gate stack prepared in situ rapid thermal chemical vapor deposition process for advanced gate dielectrics. *Journal of Applied Physics* **92** 2807.

LEHMANN, P. and OR, D. (2012). Hydromechanical triggering of landslides: From progressive local failures to mass release. *Water Resources Research* **48**.

LI, S., GLEATON, J. and LYNCH, J. (2019). What is the shape of a bundle? An analysis of Rosen's fibrous composites experiments using the chain-of-bundles model. *Scandinavian Journal of Statistics* **46** 59–86.

LI, S. and LYNCH, J. (2011). On a threshold representation for complex load-sharing systems. *Journal of Statistical Planning and Inference* **141** 2811–2823.

LI, S. and LYNCH, J. (2019). A Sketch of Some Stochastic Models and Analysis Methods for Fiber Bundle Failure under Increasing Tensile Load. <https://arxiv.org/abs/1903.02546>.

MCKENNA, K. P. and SHLUGER, A. L. (2011). Electron and hole trapping in polycrystalline metal oxide materials. *Proceedings of the Royal Society, A* **467** 2043–2053.

MISHNAEVSKY, L. (2013). 9 - Micromechanical modelling of wind turbine blade materials. In *Advances in Wind Turbine Blade Design and Materials*, (P. Brøndsted and R. P. L. Nijssen, eds.). *Woodhead Publishing Series in Energy* 298 - 324. Woodhead Publishing.

NEKRASHEVISH, S. S. and GRITSENKO, V. A. (2014). Electronic structure of silicon dioxide (A review). *Physics of the Solid State* **56** 207–222.

NTENGA, SAÏDJO, BEDA and BÉAKOU (2019). Estimation of the Effects of the Cross-Head Speed and Temperature on the Mechanical Strength of Kenaf Bast Fibers Using Weibull and Monte-Carlo Statistics. *Fibers* **7** 89.

ORGÉAS, L., DUMONT, P. and CORRE, S. L. (2015). 5 - Rheology of Highly Concentrated Fiber Suspensions. In *Rheology of Non-Spherical Particle Suspensions* (F. Chinesta and G. Ausias, eds.) 119 - 166. Elsevier.

PEREVALOV, T. V., GRITSENKO, V. A., ERENBURG, S. B., BADALYAN, A. M., WONG, H. and KIM, C. W. (2007). Atomic and electronic structure of amorphous and crystalline hafnium oxide: X-ray photoelectron spectroscopy and density functional calculations. *Journal of Applied Physics* **101** 053704.

PHOENIX, S. L. (1983). Statistical Modeling of the Time and Temperature Dependent Failure of Fibrous Composites. In *Proceedings of the Ninth U.S. Natural Congress of Applied Mechanics*. The American Society of Mechanical Engineers.

PHOENIX, S. L. and TIERNEY, L.-J. (1983). A statistical model for the time dependent failure of unidirectional composite materials under local elastic load-sharing among fibers. *Engineering Fracture Mechanics* **18** 193–215.

PIRROTTA, O., LARCHER, L., LANZA, M., PADOVANI, A., PORTI, M., NAFRIA, M. and BERSUKER, G. (2013). Leakage current through the polycrystalline HfO<sub>2</sub>: Trap densities at grains and grain boundaries. *Journal of Applied Physics* **114** 134503.

PUGNO, N. (2014). Chapter 18 - A Review on the Design of Superstrong Carbon Nanotube or Graphene Fibers and Composites. In *Nanotube Superfiber Materials* (M. J. Schulz, V. N. Shanov and Z. Yin, eds.) 495 - 518. William Andrew Publishing, Boston.

REIWEGER, I., SCHWEIZER, J., DUAL, J. and HERRMANN, H. J. (2009). Modelling snow failure with a fibre bundle model. *Journal of Glaciology* **55** 997–1002.

ROSEN, B. W. (1964). Tensile failure of fibrous composites. *AIAA Journal* **2** 1985–1991.

ROSEN, B. (1965). Mechanics of composite strengthening. In *American Society*

of Metals. Chapter 3.

SMIRNOVA, T. P., YAKOVKINA, L. V., KITCHAI, V. N., KAICHEV, V. V., SHUBIN, Y. V., MOROZOVA, N. B. and ZHERIKOVA, K. V. (2008). Chemical vapor deposition and characterization of hafnium oxide films. *Journal of Physics and Chemistry of Solids* **69** 685–687.

STRONG, A. W., WU, E. Y., VOLLERTSEN, R.-P., SUNE, J., LA ROSA, G., RAUCH III, S. E. and SULLIVAN, T. D. (2009). *Reliability Wearout Mechanisms in Advanced CMOS Technologies*. John Wiley & Sons, Ltd, Hoboken, N.J.

TAYLOR, H. M. (1987). A Model for the Failure Process of Semicrystalline Polymer Materials under Static Fatigue. *Probability in the Engineering and Informational Sciences* **1** 133–162.

VANDELLI, L., PADOVANI, A., LARCHER, L. and BERSUKER, G. (2013). Microscopic Modeling of Electrical Stress-Induced Breakdown in Poly-Crystalline Hafnium Oxide Dielectrics. *IEEE Transactions on Electron Devices* **60** 1754–1762.

ZHANG, X.-Y., HSU, C.-H., LIEN, S.-Y., WU, W.-Y., OU, S.-L., CHEN, S.-Y., HUANG, W., ZHU, W.-Z., XIONG, F.-B. and ZHANG, S. (2019). Temperature-Dependent  $\text{HfO}_2/\text{Si}$  Interface Structural Evolution and its Mechanism. *Nanoscale Research Letters* **14** 83.

ZWEBEN, C. and ROSEN, B. W. (1970). A statistical theory of material strength with application to composite materials. *Journal of the Mechanics and Physics of Solids* **18** 189–206.